SCALABLE AND LOW-COST MICRO-MESH WICKING STRUCTURES: FROM CAPILLARY EVAPORATION TO ULTRA-THIN THERMAL GROUND PLANES

by

SHANSHAN XU

B.S., Beihang University, 2013

M.S., University of Colorado Boulder, 2015

A thesis submitted to the

Faculty of the Graduate School of the

University of Colorado in partial fulfillment

of the requirement for the degree of

Doctor of Philosophy

Department of Mechanical Engineering

2017

This thesis entitled:

Scalable and Low-Cost Micro-Mesh Wicking Structures:

From Capillary Evaporation to Ultra-Thin Thermal Ground Planes

written by Shanshan Xu

has been approved for the Department of Mechanical Engineering

_____

Prof. Ronggui Yang

_____

Prof. Y.C. Lee

Date_____

The final copy of this thesis has been examined by the signatories, and we find that both the content and the form meet acceptable presentation standards of scholarly work in the above mentioned discipline.

Abstract

Xu, Shanshan (Ph.D., Mechanical Engineering)

Scalable and Low-Cost Micro-Mesh Wicking Structures: From Capillary Evaporation to Ultra-Thin Thermal Ground Planes

Thesis directed by Professor Ronggui Yang

Power electronics have become important components in low to high voltage electrical devices including portable electronics, inverters for concentration photovoltaic cells, light-emitting-diode (LED), and electric vehicles. Emerging technologies implementing wide bandgap materials such as SiC and GaN enable smaller and more compact devices with higher power density, this calls for more efficient thermal management technologies with matched ultra-thin form factors. Thermal ground planes (TGPs) utilizing phase-change heat transfer to achieve high thermal conductance offer a promising solution. However, both performance limitations and fabrication challenges are encountered when the thickness of TGPs becomes less than 0.50 mm. Capillary evaporation is the key determinant of the thermal performance of TGPs. The onset of nucleate boiling has been shown to significantly reduce the evaporator thermal resistance. However, it is challenging to maintain stable nucleate boiling in the wicking structures of ultra-thin TGPs. The

study of capillary evaporation on the wicking structures can lead to the design optimization of ultra-thin TGPs with improved heat transfer performance.

In the first part of this thesis, ultra-thin TGPs have been developed by using a hybrid wicking structure fabricated by bonding single-layer #500 stainless steel micro-mesh onto copper micropillars via electroplating. Such fabrication approach can encapsulate stainless steel wires with copper to prevent corrosion and create microscale structures on the surface to enhance the capillary pressure by increasing the surface areas. The assembled TGP prototypes were around 0.30-mm thick, among the thinnest TGPs in the world so far, and the footprint of TGPs was 10 cm × 5 cm. The maximum effective thermal conductivity of the best-performed TGP of the five tested prototypes was around 2600 W/m-K, more than six times that of a copper reference. This TGP device could operate with a heat load up to 10.5 W without dryout over a heating area of 8 mm × 8 mm.

In the second part of this thesis, the fundamental fluid and heat transport mechanisms in the multilayer micro mesh wicking structures have been studied. A custom-made experimental setup has been developed to characterize the capillary evaporation heat transfer performance of copper micro mesh wicking structures with different sizes. In addition, liquid-wicking (capillary rate-of-rise) experiments have been conducted to determine the effective permeability and capillary force of the micro mesh wicking structures. As the thickness of micro mesh wicking structures increased from 2 layers to 4 layers, the maximum heat flux has been improved from 67.5 W/cm^2 to 102.2 W/cm^2 due to the increased cross-sectional area for liquid flow.

The onset of nucleate boiling was observed to enhance the heat transfer coefficient, with the superheat varied less than 2 °C as heat flux became greater than 50 W/cm^2. However, further increasing the thickness to six layers couldn't increase the dryout heat flux further owing to the suppressed vapor bubbles removal in thicker wicking structures. To improve the vapor bubbles removal, micro mesh wicking structures with different spacings, but similar wire diameter and the meshes studied included #100, #145, and # 200 have been employed. Finer micro mesh demonstrated higher heat transfer coefficients due to the enlarged area of thin film evaporation. However, the test samples with different pore sizes all dried out around 100 W/cm^2 because of the boiling limit. Visual inspection revealed that the effective pores for vapor venting were much smaller than the intrinsic openings of micro mesh due to stackings of micro wires, and the difference caused by mesh sizes was negligible.

Two different methods have been developed to promote the heat transfer performance of micro mesh wicking structures. The first method implemented inline-aligned micro mesh wicking structure, of which the micro-cavities formed between micro wires in the direction perpendicular to the substrate provided numerous nucleation sites and the large openings between microwires enabled fast vapor removal. The experimental results have demonstrated that the dryout heat flux was increased by 45%, and the heat transfer coefficient was increased from 9.0 W/cm^2·K to 23.5 W/cm^2·K for 4-layer # 145 micro mesh. The second method applied a nanostructured surface to increase the dryout heat flux by enhancing the liquid wicking performance. The dryout heat flux of a single-layer micro mesh wicking

structure has been improved by three times, from 13.5 W/cm^2 to 44.2 W/cm^2, Furthermore, the dryout heat flux of a four-layer micro mesh wicking structure has been improved from 102.5 W/ cm^2 to 188.6 W/cm^2.

Plans for future work are outlined based on the current findings. The next steps will be to develop a methodology to precisely control the alignment of micro mesh, explore other geometric designs for enhancing heat transfer performance of capillary evaporation on thick wicking structures, and develop generalized and analytical models to predict the heat transfer performance and critical transitions in copper micro mesh wicking structures.

Acknowledgements

I express my whole-hearted gratitude, deep regards and sincere thanks to my Ph.D. advisors Prof. Ronggui Yang and Prof. Yung-Cheng (Y.C.) Lee for their invaluable, thoughtful, and brilliant guidance throughout my graduate studies. Their encouragement and support have been the constant source of inspiration ever since I entered this exciting field of research. I would like to thank my thesis review committee, Prof. Xiaobo Yin, Prof. Julie E. Steinbrenner, Prof. Dragan Maksimovic, and Prof. Yifu Ding. I am grateful for their feedback and advice regarding this research work.

My sincere gratitude and thanks go to all my lab mates, especially Dr. Ryan John Lewis, Dr. Rongfu Wen, Dr. Li-Anne Liew, and Dr. Dongliang Zhao for their assistance, and insightful suggestions provided at all stages of this research.

Last but not least, I'm thankful for the perpetual support and blessing of my family, especially my husband Fan Zhang and my daughter Robin Zhang, which reinforced my determination throughout my career.

Table of Contents

Contents

List of Tables

List of Figures

CHAPTER I INTRODUCTION

1.1 Thermal Management of Electronics

Power electronics have become important components in low to high power electrical devices including portable electronics, the inverters for concentration photovoltaic cells, light-emitting-diode (LED), and electric vehicles. Traditional power electronic devices are silicon-based. However, the emerging technologies are trending toward wide bandgap materials [1] such as SiC and GaN featured with smaller linewidths, thinner substrates, and higher dimensional architectures, allowing devices to become smaller and more compact while handling more power. Thus, compared to their counterpart of silicon, the power densities of these devices become much larger, and the thermal gradient across the devices are magnified. Currently, the heat generation at the device footprint has reached 100 W/cm^2 and it is projected to exceed 300 W/cm^2 in the next few years [2], which demands more efficient cooling technologies to prevent thermal damages such as performance degradation and thermal shock and to increase the lifetime. To increase the maximum operating heat load and reduce the chip temperature are among the most important factors in the thermal management design.

On the other hand, the rapid development of mobile internet drives the progress of smartphones and equally impacts the laptop industry[3]. The main developing directions of these devices are ultra-thin thickness, long battery life, stability, safety, and better user experience. Additionally, as smartphones, tablets, and laptops frequently come in contact with human skin, lower and more uniform surface temperature and quieter operation are two of the most important factors. And therefore, the ultra-thin thickness of devices and excellent lateral heat spreading become the most important factors in the design of thermal management solutions.

Active air cooling methods become impractical since they require large surface areas to dissipate heat, need additional supporting power supply equipment, and produce a lot of noise. Traditional passive cooling systems including thermal heat spreaders and heat pins have been utilized due to their advantages of zero noise and zero power consumption, but the performance of these systems largely replies on the thermal conductivity of the solid substrate because heat is dissipated by contacting the substrate surface and heat source surface. Heat pipes and vapor chambers offer a potential solution by spreading heat from a localized heating source to a larger surface area while incurring a small temperature gradient, and they have been used as heat spreaders in various electronic systems due to their high thermal conductance by taking advantage of phase-change heat transfer, which can be orders-of-magnitude larger than that of solid bulk materials, such as copper and aluminum.

1.2 Thermal Ground Planes (TGPs)

Based on a similar working principle as heat pipes and vapor chambers, the TGPs with a rectangular cross-section were recently proposed (Fig. 1.1). A TGP consists of casing material, wicking structure, vapor core and working fluid. Heat is absorbed into the wicking structure at the evaporator region through the casing, causing the evaporation of liquid permeating the wicking structure. The elevated pressure drives vapor to transport from the evaporator through an adiabatic section to the condenser in the vapor core. The heat is rejected through vapor condensation in the condenser, and the condensed liquid is then driven back to the evaporator via the capillary pressure provided by the porous wicking structure.

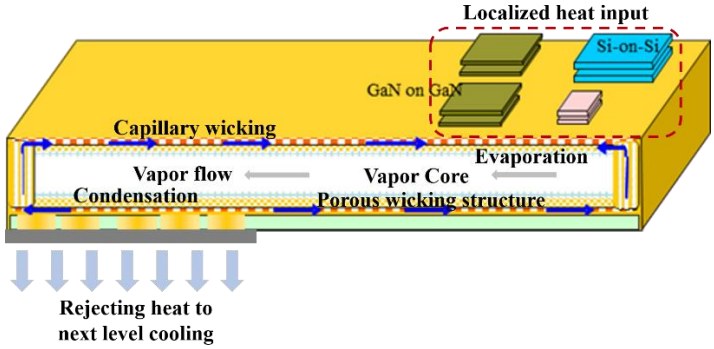

Fig. 1.1 *Operation of a TGP (liquid evaporates at the heating area, vapor condenses at the condenser region to reject the heat, and the condensed liquid is driven back to the evaporator section by capillary force provided by the porous wicking structure)*

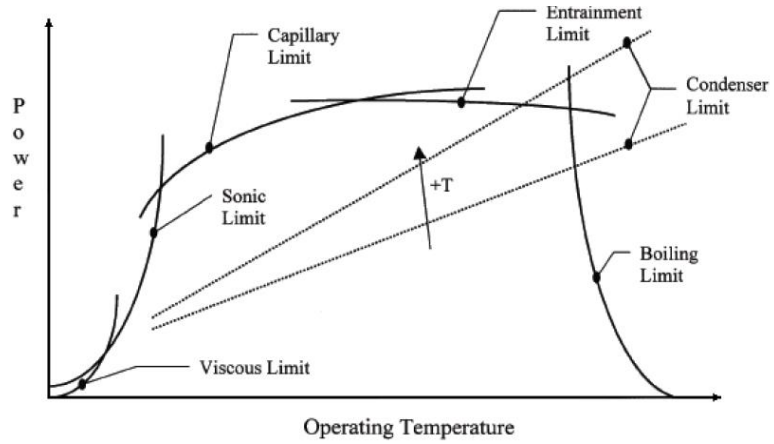

Fig. 1.2 *Various operating limitations of TGPs (capillary limit, viscous limit, sonic limit, entrainment limit, condenser limit, and boiling limit)*

TGPs have a range of operating temperatures and heat fluxes. Fig. 1.2 shows different operating limitations of TGPs including viscous limit, sonic limit, capillary limit, entrainment limit, condenser limit and boiling limit[4].

For some working fluids, such as metals and cryogenic fluids, the viscous effects dominate over inertial effects in the flow of vapor at low temperatures, and the viscous limit plays a significant role when the viscous resistance is large enough to hinder vapor flow due to the temperature differential along the length of the TGPs. The sonic limit is met when the vapor generated at the end of the evaporator reaches sonic velocity. Typically, in a TGP, the liquid and vapor transport in opposite directions. When the relative velocity of the two fluids is high, the inertial forces of the vapor tends to break the surface tension of the liquid surface. At this point, small droplets of liquid are picked up in the vapor stream, which is referred as the entrainment phenomenon.

Typically, for water-copper TGPs, the practical operating temperature [4] ranges from 25 °C to 150 °C, among which, the capillary limit is the most frequently encountered limit in the operation of TGPs. It occurs when the maximum capillary pumping pressure is less than the sum of the liquid pressure drop, vapor pressure drop, and gravitational force.

$$\Delta P_{cap} < \Delta P_l + \Delta P_v + \Delta P_{ph,e} + \Delta P_{ph,c} + \Delta P_g \tag{1.1}$$

Where ΔP_{cap}, ΔP_l, ΔP_v, $\Delta P_{ph,e}$, $\Delta P_{ph,e}$, and ΔP_g represent capillary pressure, liquid pressure drop, vapor pressure drop, pressure drop at the liquid-vapor interface at evaporator section, pressure drop at the liquid-vapor interface at condenser section, and gravitational force.

For the capillary limit of wicking structures, there are mainly two control properties: the liquid pressure drop (P_l) and capillary pressure (P_c). The capillary pressure is expressed using Young-Laplace equation[4],

$$\Delta P_c = \frac{2\sigma_l \cos(\theta)}{r} \tag{1.2}$$

where σ_l, θ, and r represent the surface tension of the working fluid, liquid-solid contact angle, and pore radius, respectively.

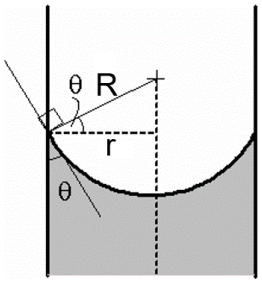

Fig. 1.3 *The schematic of a hydrophilic meniscus with wetting angle less than 90* °

The liquid pressure drop for one-dimensional axial flow through porous media can be expressed by Darcy's law[4],

$$\frac{dP}{dx} = -\frac{\mu_l \dot{m}_l}{\rho_l A_w K} \tag{1.3}$$

where μ_l, $\dot{m}_l$, ρ_l, and A_w represent the dynamic viscosity of working fluid, mass flow rate of working fluid, density of working fluid, and cross-sectional area of the wick, respectively. The wicking structure with a smaller pore radius can generate higher capillary force to drive liquid flow, however, the reduced permeability (K) can lead to a higher liquid pressure drop along the wicking structures.

Another common physical limitation for TGPs is the boiling limit. From the conventional view of point, the nucleate boiling should be avoided in TGPs having longitudinal groove or micro pillar arrays wicking structures for that in these wicking structures, the nucleation of vapor bubbles can obstruct the noncommunicating individual flow paths of liquid returning to the evaporator section, and therefore the onset of nucleate boiling is the boiling limit. Alternatively, wicking structures such as sintered powder and micro mesh with the stochastically connected network can continue to supply liquid to the heater area during boiling. For these wicking structures, boiling limit describes vapor blanketing of the surface.

The materials of TGPs are typically governed by the operating temperature of the device, a figure of merit number has been derived by balancing the capillary pressure and total pressure drop, which results in a single grouping of thermophysical liquid properties given by [5]

$$M_f = \frac{\sigma_l h_{fg} \rho_l}{\mu_l} \tag{1.4}$$

TGPs with a higher value of M_f can operate until a larger heat load prior to reaching the capillary limit. A higher surface tension yields a higher capillary pressure, while higher liquid density and latent heat reduce the liquid volume flow rate for a given power input, and a lower viscosity leads to a lower flow resistance in the wicking structures. In general, the working fluids include alcohols, ammonia, sodium, and liquid metals. Of these, water has the highest figure of merit in the temperature ranging from 25 to 100 °C, which is in the range of the mostly encountered saturation temperatures for electronics cooling technologies. TGPs using water as working fluid are typically constructed of copper materials because water is incompatible with other materials such as aluminum or stainless steel. And therefore, current work focused on water-copper based systems.

Numerical investigations have been conducted on the design of TGPs in ultra-thin scale with a thickness of submillimeter[6][7][8]. Ranjan *et al.* [8] developed a numerical model to estimate the dependence of the heat transfer performance and the total flow pressure drop of ultra-thin TGPs on the thickness of vapor core and wicking structure. They reported that when the thickness of the vapor core was in the range of 0.2-0.4 mm, the vapor space offered significant thermal and flow resistances. 0.05-mm thick wicking structures were optimal for applications when the heat fluxes were below 50 W/cm^2, while wicking structures with a moderate thickness of 0.1 mm performed best at heat flux greater than 50 W/cm^2. A TGP with thicker

vapor space and higher condenser side temperature was recommended for the use of ultra-thin TGP in heat dissipation. Yadavalli *et al.* [9] assessed the performance of submillimeter thick TGPs operating at low heat flux (<2 W/cm^2) as a function of heat input and geometric parameters by using a reduced-order thermal resistance network model and a higher-fidelity numerical model. A vapor-phase figure of merit was defined for selecting the working fluid because the smallest TGPs thickness at low heat fluxes was governed by the vapor properties, which were typically neglected in the common figure of merit that tried to maximize the capillary limit. Patankar *et al.* [10] explored the selection of working fluids for ultra-thin TGPs with a thickness in the range of 50 – 100 μm that operate with a heat load up to 7 W. The criteria were to minimize the thermal resistance while ensuring a capillary limit was not reached. A resistance-network-based model was used to develop a simple analytical relationship for the thermal resistance as a function of the working fluids properties, operating power, and the geometry.

Leveraging the advantage of micro- and nano-fabrication techniques, other investigators have made ultra-thin TGPs devices and experimentally characterized their heat transfer performance. Ding *et al.* [11] designed a novel 30 mm × 30 mm × 0.6 mm-thick titanium-based TGP with a maximum effective thermal conductivity of 350 W/m·K under a heat load of 7.5W. About 200-nm hairlike nanostructured titania was grown on arrays of micro-fabricated titanium pillars to form hydrophilic nature of the wicking structure, and the hermetic seal was formed by laser welding two micro-fabricated titanium substrates together. Lewis *et al.* [12] developed a 0.5-mm

thick TGP using double-layer copper micro mesh as the wick structure and investigated the effects of size scaling of the evaporator and condenser, and the overall TGP sizes on the thermal resistances of TGP. A thinner device with a thickness of 0.3-mm [13] was developed by using polymer materials. A graded hybrid wicking structure with pore sizes specifically optimized at different sections has been designed, and an ultra-thin titania film was deposited over the polymer materials via atomic layer deposition, acting as both a moisture barrier and a hydrophilic coating. The thermal conductivity was measured up to 541 W/m · K under an applied power of 9.54 W over an 8 mm × 8 mm heating area.

Table 1. 1 *Summary of experimental investigations of TGPs*

Authors	Wick structures	Wick thickness (μm)	Working fluids	Active area (cm × cm)	Device thickness (mm)	Heater size (mm × mm)	Dryout heat flow (W)	Thermal conductivity ($Wm^{-1}K^{-1}$)
Ding et al. [11][14]	Nanostructured Ti micro pillars	50	Water	3 × 3	0.60	5 ×30	7.2	350
Oshman et al.[15]	Cu micro-mesh on micropillars	-	Water	6 × 3	~ 1	10 × 10	11.94	830
Oshman et al.[16]	Triple-layer Cu micro-mesh	-	Water	9.5 × 5	1.31	8 × 8	25	1840
Oshman et al.[17]	Cu micro-mesh on micropillars	~ 200	Water	3 × 3	1.2	8 × 8	40	1653
Lewis et al. [12]	Cu micro-mesh	200	Water	6 × 2 10 × 5	0.5	Various heaters	5.5	1200
Lewis et al.[18]	Graded polymer micro pillars	50	Water	6 × 2	0.30	10 × 20	9.5	541
Liew et al.[19]	Triple-layer Cu micro-mesh	-	Water	9.5 × 5	1.1	25.4×25.4	26	800
Li et al.[20]	Sintered powder	various	Water	L: 20	D: 1 ~ 1.5	30×30	25	-
Li et al.[21]	Sintered powder	0.5-1	Water	10 × 5	2	12 × 10	120	~1200
Cai et al. [22]	Si micropillars	300	Water	3.8 × 3.8	3	30 × 4	-	2500
Cai et al. [23]	Si micropillars	250	Water	1 × 0.2	2	2 × 2	12	-
Cai et al. [24]	Si micropillars	150	Water	7 × 5	1	5 × 8	-	10,000
Tang et al. [25]	Sintered particle	-	Water	9 × 9	3	10 × 10	300	-

1.3 Capillary Evaporation on Porous Wicking Structures

Capillary evaporation is the key to the thermal performance of TGPs and vapor chambers. It is a thin-film evaporation based heat and mass transfer process that utilizes capillary suction to deliver liquid to the liquid-vapor free surface existing at the top layer of the porous wicking structure, and the steady thin film decreases the thermal resistance between the hot solid substrate and the liquid-vapor interface, maximizing the dissipated heat flux and heat transfer coefficient. The rate of capillary evaporation in a wicking structure is determined by three mass transport processes: (a) liquid transport to the liquid/vapor interface; (b) liquid vaporization at the liquid/vapor interface; and (c) the removal of generated vapor. The maximum dissipated heat flux is referred to dryout heat flux in capillary evaporation.

Several studies have developed facilities to reproduce and investigate such capillary evaporation phenomenon from wicking structures. As shown in Fig. 1.5, the bottom of the sample was submerged into a bath of working fluid, and the working fluid was driven to the heater area by capillary action. The heat transfer coefficient/thermal resistance could be calculated by the applied heat flux to the wicking structures and the temperature difference between the heated substrate and the vapor space.

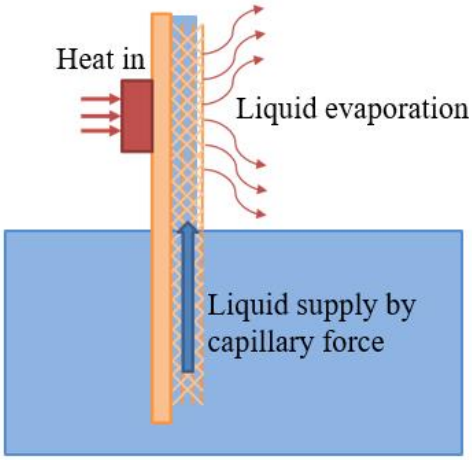

Fig. 1.4 *The schematic of the capillary evaporation characterization test setup*

Capillary pore radius and permeability are two of the most important parameters that determine the capillary performance of porous wicking structures. There are several available methods for evaluating the provided capillary pressure of wicking structures. These methods focus on determining the effective pore radius of the wicking structure which can be used to calculate the capillary pressure for any liquid provided the properties and wetting characteristics are known. Bubble-point method [26] forces a compressed gas at known pressure through a porous media saturated with the test liquid; the pore radius can be determined based on the minimum pressure that causes the gas to pass through the sample as a bubble. However, this method characterizes the pore radius using a single pore size that is determined from the largest pore flow path. And it becomes rather inadequate since the maximum capillary pressure is defined by the minimum pore size. Another method for determining the capillary pore radius is [4] using a plug of wicking material to hold a column of liquid against an applied gravitational head, the liquid column will break when the gravitational head is increased to the maximum provided

capillary pressure. A static liquid rise technique [4] introduces the lower edge of a porous material to a liquid bath and allows the material to wick fluid against gravity until it reaches a static maximum height corresponding to the provided capillary pressure. One disadvantage of this method is the sample itself must be long enough for static equilibrium to be observed, in addition, the experiments must be conducted in a completely saturated environment due to the important role of evaporation as the liquid gradually reaches static equilibrium. An alternative method is referred as a rate of rise test[27][28], which measures the transient change of liquid by either direct visualization or weight. By modeling these capillary flow dynamics, a factor such as K/R_{eff} or $\Delta P_{cap} \cdot K$ can be obtained which contains the key parameters governing the flow.

The permeability of a wicking structure can be measured in forced flow tests by measuring the pressure drop across a porous material for a given flow and known area through which the liquid is passing. The flow can be radial in-plane, linear in-plane, or linear through-plane[26]. The fluid can be either gas or liquid. Adkins *et al.* [29] flowed liquid radially through a felt wicking material and measured the pressure drop to determine the permeability of wicking structures with various thicknesses. A similar technique was used by Williams and Harris [30] later. Kozai *et al.* [31] used linear flow technique to investigate the permeability of metal micro mesh wicking structures. A constant pressure source was used to provide flow through a rectangular sample clamped between two sealing surfaces. An expression was developed to predict the permeability of metal micro mesh based on compression, wire

diameter and spacing dimensions. A similar approach was employed by Noda *et al.* [32]to determine the dependence of permeability on the porosity of a micro mesh wicking structure. Zhang *et al.* [33] utilized a syringe pump to impose a fixed flow through the system and measured the pressure difference to study the effect of sintering conditions on the permeability of copper inverse opal wicking structures.

In the above discussion, two different experimental setups are required to obtain the effective capillary radius and permeability. However, under certain conditions, both capillary pressure and permeability can be extracted from the rate-of-rise experiments [34][35]: (a) the flow is one-dimensional, (b) no friction or inertia effects in the liquid reservoir, (c) the viscous pressure loss inside the wicking structure is given by the Hagen-Poiseuille. A general describing function can be expressed as:

$$\frac{dh}{dt} = \frac{2K\sigma_{lv}\cos\theta}{R\mu\varepsilon}\frac{1}{h} - \frac{\dot{m}_{evap}}{2d\rho\varepsilon}h - \frac{g\rho K}{\mu\varepsilon} \tag{2.1}$$

The function can be further reduced to (2.2) when the rate-of-rise experiments are conducted inside a sealed chamber so that the evaporation effect can be neglected.

$$\frac{dh}{dt} = \frac{2K\sigma_{lv}\cos\theta}{R\mu\varepsilon}\frac{1}{h} - \frac{g\rho K}{\mu\varepsilon} \tag{2.2}$$

By non-linear regression, both capillary pressure and permeability can be extracted. However, this method is only valid when the gravitational term $\frac{g\rho K}{\mu\varepsilon}$ cannot be neglected, otherwise, only a factor of K/R_{eff} or $\Delta P_{cap} \cdot K$ can be achieved.

The capillary evaporation performance of a variety of microstructures and nanostructures have been studied by different studies, as summarized in Table 1.2.

Table 1. 2 *Summary of recent experimental investigations on capillary evaporation*

Authors	**Wick structures**	**Wick thickness**	**Test fluids**	**Heater size**	**Wicking length**	**Maximum heat**
Micro pillars wicking structures						
Adera et al.[2]	Silicon micropillars Pillar dia: 8-12 µm Pillar pitch: 12-20µm	0.031-0.090mm	Water	10mm × 10mm	Horizontal	~ 92W/cm^2
Adera et al.[36]	Silicon micropillars Pillar dia: 6-7 µm Pillar pitch: 20-50µm	0.030-0.090mm	Water	10mm × 10mm	Horizontal	~ 46W/cm^2
Zhu et al.[37]	Silicon micropillars Pillar dia: 5-12 µm Pillar pitch:12-20µm	0.019-0.020mm	Water	10mm × 10mm	5-10mm	~ 46W/cm^2
Tej et al. [38]	Silicon micropillars Pillar dia:15 µm Pillar pitch: 30-50µm	0.100mm	Water	10 mm × 20 mm	20-50mm	~ 13W
Ravi et al.[39]	Silicon micropillars Pillar dia: 15 µm Pillar pitch: *30-50µm*	0.100-0.150mm	Water	10 mm × 20 mm	20-55mm	~18W
Sintered powder/particle wicking structure						
Hanlon and Ma[40]	Monoporous sintered copper powder Particle dia. 635 µm Porosity: 0.43	1.9-5.7mm	Water	10mm × 20mm	Horizontal	~ 35-55 W/cm^2
Davis and Garimella [41]	Monoporous sintered copper powder Particle dia.: 635 µm Porosity: 0.43	1 mm	Water	384 mm^2	Horizontal	~ 30-33 W/cm^2
Semenic et al[42]	Monoporous sintered copper powder Particle dia.: 53-710 µm Porosity: 0.318-0.371	1mm	Water	70.9 mm^2	Horizontal	209-223 W/cm^2
Weibel et al[43]	Monoporous sintered copper powder Particle dia.:60-302.5 µm Porosity: 0.635-0.657	0.6-1.2mm	Water	5mm × 5mm 10mm × 10mm	8.25mm	500-596.5W/cm^2

Table 1.2 *Summary of recent experimental investigations on capillary evaporation-cont'd*

Biporous/Hybrid wicking structure						
Weibel et al[44]	Monoporous sintered copper powder Particle dia.: 100 μm Porosity: 0.5	0.2mm	Water	5mm × 5mm	8.25mm	160-430W/cm^2
Adera et al.[45]	Biporous silicon pin fins with vertical microgrooves Pin dia.: 4.6-7.7μm Pin pitch: 20μm Groove width.:52μm Pin cluster width.: 50 μm	0.022-0.024mm	Water	10 mm × 10 mm	Horizontal	102 W/cm^2
Ravi. et al.[46]	Segmented micro pillars Pillar dia. 10-42 μm Pillar pitch.10-48μm Adiabatic pillar dia.:42 μm Pillar pitch.48-88μm	0.1mm	Water	10 mm × 20 mm	20-45mm	~17W/cm^2
Ravi. et al.[46]	Micro mesh on micropillars Mesh dia. 4-20 μm Pillar dia.15-42μm	0.101-0.280mm	Water	10 mm × 10 mm	20-45mm	~22W/cm^2
Dai et al[47][48][49]	Micro mesh on copper micro channels Mesh dia. 56 μm Mesh spacing:100μm Channel width: 250 μm	0.32mm	Water	10 mm × 10 mm	Vertical 15 mm	152.2 W/cm^2
North et al[50]	Biporous sintered copper powder Particle dia.: 66-89 μm Cluster dia.: 250-710 μm Porosity: 0.70	0.64mm	Water	30 mm × 8 mm	Horizontal	20-70 W/cm^2
Semenic et al[51]	Biporous sintered copper powder Particle dia.: 29-63 μm Cluster dia:250-710 μm Porosity: 0.597-0.631	1-4mm	Water	70.9 mm^2	Horizontal	150-494W/cm^2
Semenic et al[51]	Biporous sintered copper powder Particle dia.: 41-83 μm Cluster dia:302-892 μm Porosity: 0.51-0.68	0.8-23m	Water	32.2 mm^2	Horizontal	244-990W/cm^2

Table 1.2 *Summary of recent experimental investigations on capillary evaporation-cont'd*

Zhao and Chen [52]	Sintered copper powder with vertical microgrooves Particle dia. 50 μm Groove width:150 -500μm Bank width:250-500 μm	2mm	Water	5 mm × 5 mm	7-20mm	200-350W/cm²
Hwang et al. [53]	Oxidized sintered copper powder with capillary artery posts Particle dia. 60 μm Artery pitch 3.52mm	0.06mm	Water	10mm × 10 mm	Distributed liquid return	387W/cm²
Hwang et al. [54]	Sintered copper powder with converging lateral arteries Particle dia. 60 μm	0.06 mm	Water	10mm × 10mm	45mm	580W/cm²
Ju et al[55]	Sintered copper powder with converging lateral arteries Particle dia. 60 μm	0.06mm Artery 1.5mm	Water	10mm × 10mm	45mm	350-400W/cm²
Weibel and Garimella [44]	Sintered copper powder with radial and square grid converging arteries Particle dia. 100 μm Porosity 0.5 0.5mm wide arteries	1mm	Water	5mm × 5mm	8.25mm	437-558W/cm²
Coso et al.[56]	Biporous silicon pin fins with vertical microgrooves Pin dia. 3.1-29μm Pin pitch 4.9-28μm Groove width.:30-61μm Pin cluster width.: 156 -288 μm	0.135- 0.243 mm	Water	2.5mm × 2.5mm 10mm × 10mm	5mm	73.6-733.1W/cm²
Cai and Chen[22]	Carbon nanotube (CNT) biwick with vertical microgrooves CNT dia < 20nm Groove width 50 μm CNT cluster width:100μm	0.250mm	Water	2mm × 2mm	5mm	600W/cm²

Table 1.2 *Summary of recent experimental investigations on capillary evaporation-cont'd*

Cai and Bhunia[57]	CNT biwick with vertical microgrooves or micro pillar clusters CNT dia < 20nm Groove width: 50 μm CNT cluster width: 100-250μm	0.250mm	Water	2mm × 2 mm 10mm × 10 mm	9-10mm	130-770W/cm²
Nam et al.[58]	Copper oxide nanostructured copper micro pillars Pillar dia. 50 μm Pillar pitch: 20-50 μm	0.100mm	Water	2mm × 2 mm 5mm × 5 mm	15mm	125-800 W/cm²
Weibel et al[59]	Copper-functionalized CNT-coated sintered copper powder with square grid converging arteries CNT dia. 100nm Particle dia:100 μm	0.2-1mm	Water	5mm × 5 mm	8.25mm	450-530W/cm²
Kousalya[60]	Copper-functionalized CNT-coated sintered copper powder with square grid converging arteries CNT dia.: 85-275nm Particle diameter:100μm Porosity: 0.5	0.2mm	Water	5mm × 5 mm	8.25	350-450W/cm²
Micro mesh wicking structures						
Brautsch and Kew[61]	Stainless-steel mesh, wire dia. 40 -190 μm porosity 0.313-0.469	1-5 layers	Water	Variable area (not reported)	55-79mm	8.24 – 21.39W/cm²
Li et al.[62]	Sintered copper mesh Wire dia. 56 μm Porosity 0.693-0.737	0.21-0.74mm	Water	8 mm × 8 mm	Horizontal	150-367.9 W/cm²
Li et al.[63]	Sintered copper mesh Wire dia. 56-191μm Pore 119.3-232.8 μm Porosity 0.409-0.692	0.37 mm	water	8 mm × 8 mm	Horizontal	150-367.9W/cm²
Diao et al.[64]	Sintered copper mesh Wire dia. 66-118μm Pore 134-408 μm	0.6-1.0mm	Water	Diameter: 29mm	Vertical (not reported)	~ 75W

Micropillar wicking structures have been systematically studied since the geometry of micro pillars can be well-defined by micro fabrication techniques. The fluid transport properties have been extensively studied by numerical simulation, and semi-analytical models have been developed to optimize the design of micro pillar arrays[65]. Yazdchi *et al.* [66][67] numerically studied the permeability of cylinder micro pillar arrays and created a hybrid equation. Tamayol and Bahrami [68] used cell approaches to model actual pillar arrays as opposed to long cylinder arrays. Ranjan *et al.* [69]used numerical simulations to develop correlations for pillar array permeability as a function of porosity for different pillar shapes. Xiao and Wang [70] and Byon and Kim [71] formulated numerical approximations for permeability of micropillar arrays of finite-height using Brinkman's equation. The software SURFACE EVOLVER was used to compute the shape of the liquid meniscus in a unit cell of the micro pillar array based on an energy minimization algorithm. For given pillar diameter and pitch, the correlations for the liquid volume filling the microstructure as well as the meniscus area were obtained by the meniscus shape. Zhu *et al.* [37] developed a model numerically simulates liquid velocity, pressure and meniscus curvature along the wicking direction by conservation of mass, momentum, and energy based on a finite volume approach, the dryout condition was determined when the minimum contact angle on the pillar surface reached the receding contact angle as the applied heat flux increased. The effects of micro pillar array geometries including diameter, pitch, and height on the dryout heat flux have been studied. Adera *et al.* [36] developed a semi-analytical model to determine the capillary dryout

heat flux and wall temperature, and they have also performed systematic experiments to characterize capillary evaporation from silicon micro pillar array wicking structure. The maximum heat flux was 46 W/cm^2 for the heater with size of 1 cm × 1 cm, and nucleate boiling wasn't observed. The experimental results were further compared to the results tested under ambient environment [2], which increased the figure of merit by a factor of two, leading to an increase in the dryout heat flux. In these tests, the wicking structures dried out before nucleate boiling occurred in the samples, so the experimental results tested under both saturated and ambient environment agreed well with that predicted by semi-analytical modeling. Numerical methods have provided some insights for the optimization of geometric parameters of micro pillar wicking structure. However, there are limitations to numerical methods. For one thing, numerical modeling doesn't account for nucleate boiling; it only considers thin film evaporation. For instance, in the study of Adera *et al.* [36][2], nucleate boiling was not observed for all the test articles due to relatively thin wicking structure (thinner than 100 μm) and relatively low heat fluxes (less than 100 W/cm^2). For another thing, the geometry of wicking structures needs to be perfectly regular so that only one unit cell needs to be considered to save computational time and cost. Furthermore, high-aspect-ratio micropillars are required in order to achieve high maximum heat flux, which becomes rather challenging when the copper material is employed. In general, while the geometry of micro pillar arrays can be optimized by numerical simulations, it is not practical due

to the difficulties in fabrication and the high cost resulting from processing. Moreover, numerical simulation becomes invalid when boiling occurs as the heat flux increases.

The sintered metal powder is another commonly used monoporous wicking structure. Hanlon and Ma [40] investigated the liquid film evaporation and capillary wick thickness effects for sintered copper particle beds, and found that thin film evaporation on the top surface of the wicking structure was the key factor in the improvement of the heat transfer efficiency of the capillary wick and that an optimum thickness existed for a given particle size. Chien and Chang [72] evaluated the thermal resistance of sintered powder wicking structures by using water as working fluid. The average particle diameters of sintered powders were 115 and 247 μm, and the thicknesses were 0.55 and 0.95 mm were, and it was reported that an optimum layer thickness-to-particle diameter ratio existed. For the cases where the sample was submerged in the water, an intermediate value of the thickness-to-particle diameter ratio in the range studied of 3.85 (0.95mm/247μm) yielded to the optimum performance. Zhao and Chen [73] evaluated the boiling resistance, and the maximum performance limitations of sintered powder wicking structures, both the dryout heat flux and thermal resistance performance were found to be superior for a particle of diameter of 50 μm with a thickness of 0.5 mm, compared to a 3 mm thick layer, the thinner layer demonstrated a maximum heat flux larger than 100 W/cm^2, however, the performance was strongly related to the distance between the water reservoir and the heater region, suggesting that the maximum heat flux may be governed by the capillary limit. Weibel *et al.* [43] investigated the capillary evaporation/boiling

performance of sintered copper powder wicking structures, and demonstrated that for a given wick thickness, an optimum particle size existed which maximized the boiling heat transfer coefficient, and nucleate boiling from the wicking structure led to substantially enhanced performance as compared to evaporation from the liquid-vapor free surface. It was clear that for sintered copper powder/particles, there existed an optimum ratio between the pore size and thickness which could lead to the best thermal performance. Palko *et al.* [74] demonstrated heat dissipation exceeding 1200 W/cm^2 by boiling water from volumetrically Joule heated thin (< 40 μm) porous copper inverse opal wicking structures of uniform pores of 5 μm with lateral dimensions of 2 mm × 0.3 mm, superheats were shown to be less than 10 K at maximum dissipation and varying less than 5 K over input heat flux ranges of 1000 W/cm^2. Such superior superheat performance was attributed to fine feature sizes of 5 μm. However, the low permeability of such wicking structures limited the length scales over which these structures can be implemented. While sintered metal powder has the merit of high thermal conductivity and capillary pressure induced by closely packed fine powders, the low permeability prevents their applications over large length scales. Furthermore, the high temperature required for sintering makes them rather challenging to be integrated into the microsystems and electronic devices.

The competition between capillary driving force, which scales inversely with feature size, and the viscous resistance, which scales inversely with the square of feature size, and the desire to operate at larger wicking lengths, often limits the feature sizes that are applied in capillary evaporation heat transfer. As is shown in

Fig. 1.5, systems may combine fine-scale features with enhanced capillary suction and coarser features for liquid transport, which are referred as biporous or hybrid wicking structures.

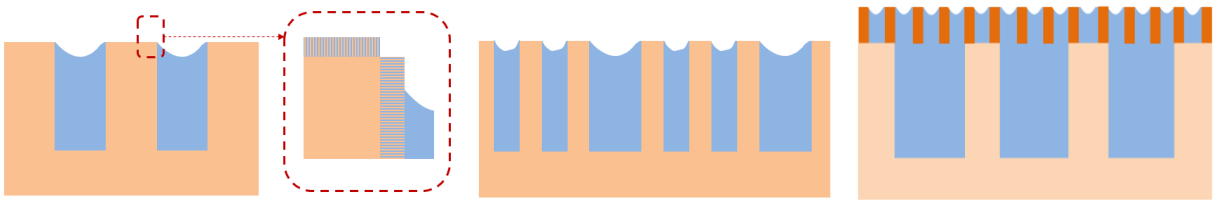

Fig. 1.5 *Schematic illustrations of different hybrid wicking structures (a) hybrid wicking structure formed by the growth of nanostructures on a homogeneous wick (b) biporous wicking structures consisted of two or more distinct pore sizes (c) hybrid wicking structures with small pores at the liquid-vapor interface and large pores adjacent to the wall*

The first type involves the implementation of nanostructures on the surface of a monoporous wicking structure. Ding *et al.* [14][11] improved the wetting of titanium pillars by growing ~ 200-nm hairlike nanostructured titania on the pillar surfaces. Zuruzi *et al.* [75] also created nanostructured titania layer on titanium micropillars, which increased the capillary speed of water during spreading in the titanium micropillar arrays by slightly more than 1.6 times. Nam *et al.* [76][58] formed sharp needle-like CuO nanostructures on copper micropillars by controlled chemical oxidation, reducing the static contact angle to be below 10°, compared with a value of 46° for water on a nominally smooth CuO surface. Weibel *et al.* [59] coated sintered copper powder micro wicking structures with controlled carbon nanotube arrays,

which were shown to reduce the surface superheat temperature by as much as 72% by initiating boiling at low heat fluxes and avoiding the boiling incipience temperature overshoot observed for uncoated samples. The implementation of nanostructures can increase the capillary pressure by decreasing the contact angle while keeping the permeability nearly identical to that of the homogeneous base wicking structure. Additionally, it also increases the thin film area through the wicking effect of the nanostructures. However, this type of hybrid wicking structures only brings the heat transfer performance of the hybrid wicking structure to the theoretical limit of the homogeneous base structure. Additionally, the reliability of nanostructures remains another main concern.

Biporous or bidispersed wicking structures comprise the second type of hybrid wicking structures and consist of two or more pore sizes[77][78][52][28][79]. Lewis *et al.* [18] fabricated a graded micropillar wicking structure to optimize the pressure drop in different regions of the device. Semenic *et al.* [80] studied different biporous wicking structures with various particle and cluster diameters, wicking structure thickness, and evaporator areas. The best thin biporous wicking structures tested had critical heat flux at 520 W/cm^2 with a superheat of 50 °C, which was relatively high. Coso *et al.* [56] evaluated the heat transfer performance of biporous wicking structures consisting of microscale pin fins separated by microchannels, the highest heat transfer coefficients of 20.7 (± 2.4) W/cm^2·K were attained at heat fluxes of 119.6 (± 4.2) W/cm^2 until the wicking structure dried out in the evaporation dominated regime. In the nucleate boiling regime, heat fluxes of 277.0 (± 9.7) W/cm^2 can be

dissipated from a heater area of 1 cm^2. Biporous wicking structures are designed to facilitate efficient boiling in the wicking structure, with the large pores acting as vapor venting pathways at high heat fluxes. Therefore, these wicking structures generally operate at shorter wicking lengths where boiling is observed before the capillary limit is reached.

The third type of hybrid wicking structures are similar in configuration to the conventional compound wicks, wherein the pore sizes vary in the direction normal to the wicking structure plane. Oshman *et al.* [15][17] have implemented hybrid wicking structures formed by bonding copper micro mesh onto copper micro pillars as the wicking structures for thin flat heat pipes. Dai *et al.* [47] fabricated such a hybrid wicking structure consisting of single-layer copper micro mesh bonded to copper micro channels. The dryout heat flux was increased by 83% compared with the base micro channels wicking structure. Ravi *et al.* [46] reported that such hybrid wicking structures remained operational only when liquid was constrained within the pores of micro mesh layer; however, the recession of the meniscus just below the mesh resulted in instantaneous local dryout.

The fabrication process of monoporous or biporous (hybrid) wicking structures containing micro pillars or micro grooves/channels is rather complicated and therefore expensive, furthermore, the requirement of templates that often created by photolithography limits the overall size of the wicking structures, leading to their limited applications in thermal management devices. For wicking structures containing sintered metal powders, the sintering process requires high temperature,

making them difficult to be integrated into the printed circuit board. Micro mesh, however, is scalable and commercially available, and they can be bonded to substrate via low-temperature thermal diffusion bonding. The high permeability of micro mesh makes them ideal for large length scale applications, and the stochastic interconnected networks can continue to feed liquid to the evaporator during the boiling regime. Wang and Peterson [81] developed a two-dimensional analytical model to evaluate the capillary evaporation limitation of micro mesh wicking structure, and they concluded that the maximum capillary evaporation heat transfer was proportional to the thickness of the porous layer, and it increased with operating temperature until it reached a value of 150 °C. However, this model didn't consider the effect of nucleate boiling, so it was not applicable for micro mesh wicking structures with nucleate boiling. Furthermore, this model assumed that the whole multilayer micro mesh was homogeneous, which was almost impossible due to the difficulty to control the alignment of micro mesh wires. Kempers *et al.* [82] experimentally studied the effects of the number of mesh layers and amount of working fluid on the heat transfer performance of copper-water heat pipes with micro mesh as wicking structures. It was reported that the thermal resistance of heat pipes increased as the number of mesh layers increased. The data presented therein also demonstrated that there was only one characteristic regime in the heat transfer curve with heat load as a function of superheat for multilayer micro mesh wicking structure. However, there exist two distinct regimes for triple-layer micro mesh, which wasn't discussed by the authors. Li *et al.* [62][63] studied the effects of

thickness by changing the number of micro mesh layers, porosity by changing the compression factor, and mesh sizes on the maximum evaporation heat flux and heat transfer coefficient. The experiments were conducted horizontally, and the liquid was fed to the evaporator by capillary pumping. Unlike other studies of [81][82][83][84], the heat transfer coefficient was reported to be independent of the thickness of micro mesh wicking structure[62]. And the author concluded that the heat transfer performance was dominated by the exposed surface rather than the total surface area. Additionally, the results of the effect of mesh sizes on the maximum evaporation heat flux exhibited an opposite trend in [63] and [84][83][85]. In reviewing the recent investigations of capillary evaporation of multilayer micro mesh wicking structures, it can be concluded that the effect of geometric parameters on the heat transfer performance is not consistent in different research work.

1.4 Objective of This Thesis

There are two main objectives of current work: to development ultra-thin TGPs with effective thermal conductivity higher than a copper reference, and to further understand the fundamental fluid and heat transport in multilayer micro mesh wicking structures, commonly used in vapor chambers and TGPs, and to thereby improve the design and performance capabilities.

The thermal management of microsystems and electronics has become increasingly important due to the continuous increasing power density. TGPs which utilize phase change heat transfer to achieve high thermal conductance offer a promising solution and have been used as heat spreaders in a variety of electronic systems. Decreased thickness of handheld and mobile electronics and the thriving market of wearable electronics call for efficient thermal management devices with matched ultra-thin form factors and flexibility. However, both fabrication challenges and performance limitations are encountered when the thickness reduces to submillimeter. Current work focuses on developing ultra-thin form factor (less than 0.5-mm) TGPs for mobile electronics which target for reducing the thickness and improve skin surface temperature uniformity. Capillary evaporation plays an important role in the heat transfer performance of TGPs, and therefore it is of critical importance to characterize the capillary evaporation of micro mesh wicking structures. In current work, the dependence of dry-out heat flux and heat transfer coefficient on the geometric parameters of micro mesh wicking structure is investigated, and based on these findings, two different methods have been developed to improve the heat transfer performance of micro mesh wicking structures.

1.5 Organization of This Thesis

This thesis is organized into four chapters. Chapter 1 presents a brief overview of TGPs technology and capillary evaporation and motivates the current work. Chapter 2 presents the development of ultra-thin TGPs with effective thermal conductivity higher than copper reference. Chapter 3 discusses the test facility developed to evaluate and visualize the capillary evaporation from micro mesh wicking structures and the effects of geometric parameters of wicking structures on the fluid and thermal performance. And with these understandings, two different methods including the implementation of inline-aligned micro mesh wicking structure and nanostructured surface have been developed for enhancing the heat transfer performance of multilayer micro mesh wicking structures. Lastly, chapter 4 provides conclusions and outlines proposed future work.

CHAPTER 2 DEVELOPMENT OF ULTRA-THIN TGPS

2.1 Introduction

Power electronics are trending toward using wide bandgap materials such as GaN and SiC that enable more compact and thinner designs with more embedded functionality and performance capabilities. Due to the constrained space and increased power densities, it becomes impractical to dissipate the waste heat effectively by using active air cooling methods or heat sinks with large surface areas. Ultra-thin TGPs, passive thermal management devices with thermal conductance orders of magnitude higher than a solid piece of bulk metals such as copper and aluminum by taking advantage of latent heat of phase change, could provide a viable solution. However, the continuous shrinkage of the device thickness mandate TGPs able to operate effectively at ultra-thin thicknesses. However, as TGPs become thinner than 0.5-mm thick, both fabrication challenges and performance limitations are encountered. Furthermore, it has been demonstrated that as the TGPs become thinner, the effective thermal conductivity of TGPs decreases significantly [12][13][15][16][17][19][21][22][86][87][88][89][90][91][92][93][94][95][96][97].

In this thesis work, ultra-thin TGPs with a thickness around 0.30 mm have been developed by implementing a novel hybrid wicking structure formed by bonding

single-layer stainless steel micro mesh onto copper micropillars via electroplating, which enabled both high capillary force and high permeability to achieve high capillary limit. Copper-cladded Kapton was used as the casing material due to its flexibility and reliability, and electroplated copper pillars were used to support the casing over a vapor space. The assembled TGPs had an active area of 10 cm × 5 cm. All samples demonstrated higher effective thermal conductivity among all the powers applied compared with a copper reference. The experimental results demonstrated that a thicker vapor core and higher saturation temperature (warmer condenser) could largely enhance the heat transfer performance of ultra-thin TGPs by reducing the thermal resistance and increasing the capillary limit. Additionally, the degradation of ultra-thin TGPs has been studied by testing the same TGP after 45 days under the same test setup and it was found that there was no degradation.

2.2 Overall Geometry

The overall geometry of the ultra-thin TGPs is shown in Fig. 2.1. The casing material was copper-cladded Kapton with 0.012-mm thick copper laminated on both sides of Kapton, providing high flexibility, hermetic seal and prevent Kapton outgassing inside TGPs. The vapor spacer was formed by copper pillars, about 150 μm thick, and the wicking structure consisted of single-layer stainless steel micro mesh bonded onto copper micro pillars, the micro mesh was 50 μm thick, while micro pillars were 30 μm tall. The obtained ultra-thin TGPs are around 0.30-mm thick.

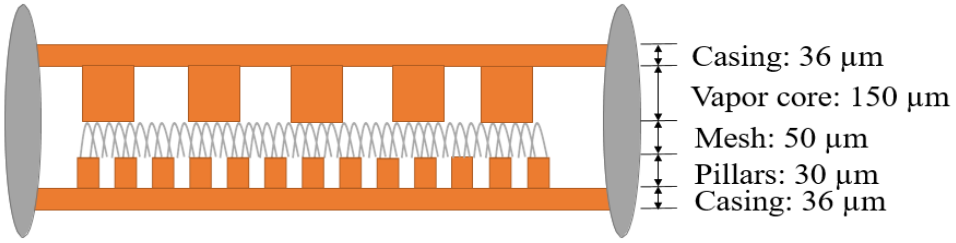

Fig.2. 1 *The overall geometry of ultra-thin TGPs with parameters of thickness*

As shown in Fig. 2.2(b), the diameter of vapor micro pillars was 1 mm, and the spacing between two pillars (center-to-center) was 2 mm. The vapor pillars were designed with eight V-shape grooves around the perimeter which defined channels to allow water that may condense along the pillars to return to the wick (as shown in Fig. 2.2 (c)) and minimized the effect of over-plating in the fabrication process. The variation in the height of vapor pillars was around 25 μm due to the processing.

The hybrid wicking structure was formed by bonding micro mesh (as shown in Fig. 2.2(d)) to square copper micro pillars. The bonding was achieved via electroplating, which not only encapsulated stainless steel micro wires to prevent corrosion of stainless steel and water, but also increased the surface area for enhancing thin-film evaporation. The width of square pillars was 100 μm, and the distance between two adjacent pillars was 60 μm (as shown in Fig. 2.2(e)).

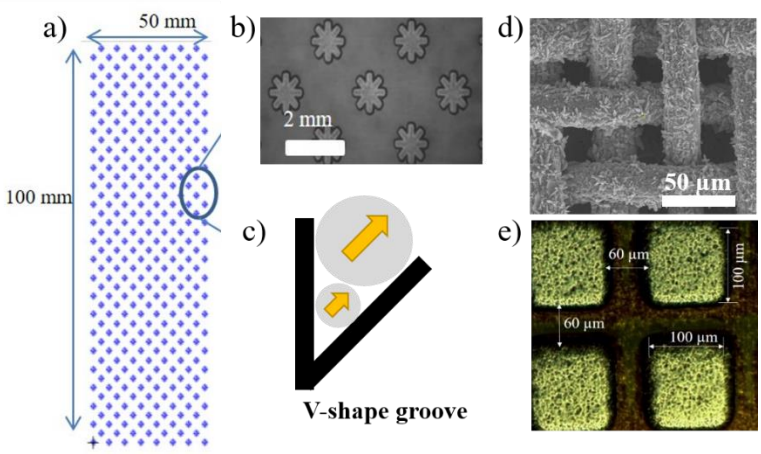

Fig.2. 2 *Details of vapor core and wicking structure (a) overall layout (b) microscope image of actual vapor pillars, grooves are visible (c) sketch of a V-shape groove drives water condensate outward by surface tension gradient (d) scanning microscope (SEM) image of stainless-steel micro mesh with microscale copper flakes (e)microscope image of copper micro pillars*

The properties of stainless steel micro mesh is given in Table 2.1, the wire's diameter was 25.4 µm, and the spacing between wires was 30 µm, the micro mesh had a porosity of 0.588 and a permeability of 6.32×10^{-12} m^2.

Table 2. 1 *Properties of the woven stainless-steel mesh*

Mesh Properties	
Wire Diameter	d_w = 0.001 inches = 0.0254 mm
Wire Spacing	w = 0.001 inches = 0.030 mm
Mesh Number	N = 500/inch = 19685/m
Overall Thickness	t = 0.002 inches = 0.0508 mm
Stainless Steel Thermal Conductivity	k_{ss} = 16.3 W/m·K
Porosity (parallel direction)	ε = 0.588
Permeability	K = 6.32×10^{-12} m^2

The fabricated vapor micro pillars and wicking structure samples are shown in Fig. 2.3(a), the micro pillars around the perimeter were taller than the rest of the vapor pillars due to current concentration effect during electroplating. As shown in Fig. 2.3(b), the TGP prototypes had an active area of 10 cm × 5 cm, and it was flexible.

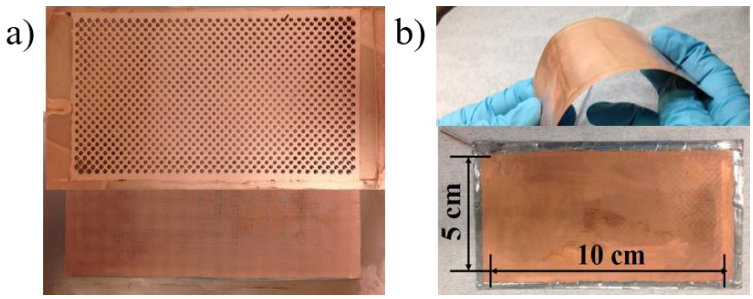

Fig.2. 3 *The photograph of obtained samples (a) the photograph of the wicking structure and the vapor core (b) the photography of a TGP prototype*

2.3 Fabrication and Assembly

2.3.1 Fabrication of Copper Pillars

The copper pillars supporting the vapor space was fabricated through a standard photolithography and electroplating process, as shown in Fig.2.4. A 36-μm thick copper-cladded Kapton sample was firstly cleaned with acetone in an ultrasonic bath for 20 min, then followed by isopropanol ultrasonic bath for 20 min to remove most of the organic residues on the surface. The sample was then dried with an air gun and cleaned in 2wt% dilute sulfuric acid solution for 30s, and rinsed with deionized water for 15 min. The copper-cladded Kapton sample was then taped to a silicon wafer of a diameter of 152.4 mm with Kapton tape which could withstand high-temperature baking on the perimeter of the sample to enhance the uniformity

of coating thickness of the photoresist. Right before spin-coating, the sample was placed on a hot plate with 110 °C for 30s to remove the moistures. The thickness of the photoresist AZ P4620 was defined in a two-step coating process. In the first coating, the photoresist was spin-coated for 500 rpm for 15 s to spread the photoresist, and then spinning at 1400 rpm for 30s. After that, the photoresist was soft-baked at 110 °C for 150s on a precise hot plate. The second-step coating followed the same speed and time interval for coating, and soft-baked at 110 °C for 240s. The obtained photoresist was about 50 μm. The photoresist was then masked and exposed to UV light at 10 mW/cm^2 for 300s. The pattern was developed in AZ 400K diluted in deionized water with a ratio of by 2.5: 1, under light agitation for a period ranging from 4 to 15 min. The period depended on the humidity and temperature in the cleanroom. A complete development was confirmed through visual inspection under the microscope. The sample was exposed to oxygen plasma for 5 min at a pressure of 1 Torr and a power of 75 W to remove any remaining photoresist residues from the exposed area before electroplating. The sample was then prepared for electroplating by taping the non-patterned copper surface, and the oxidized residues of the photo-patterned copper surface were removed by rinsing the sample with 2wt % sulfuric acid solution for 30s, followed with a thorough rinsing in deionized water for 5 min. Subsequently, the periphery of the sample was electrically connected to a DC power supply, and copper electroplating proceeded at a current of 0.20 A for 5 h, with a continuous light agitation by an oscillator with a 4 cm stroke and 4 s period. This corresponded to an initial electroplating current density of 0.004 A/cm^2; however,

after the plating thickness reached 50 μm, the copper would over-plate the pattern, reducing the current density. The over-plating time was tuned such that the final copper thickness was 150 μm. Such over-plating was unavoidable for reaching 150 μm thick pillars in this process as 50 μm was the maximum thickness at which AZ P4620 was found to be reliably photo-patternable. The thick photoresist SU-8 or AZ 125nXT was not used since processing SU-8 or AZ 125 nXT on a flexible substrate with a large area of 10 cm × 5 cm led to adhesion failure and non-uniformity of the photoresist during the processing. After electroplating, the sample was cleaned in an ultrasonic deionized water bath for at least 30 min to remove any remaining electrolytes, and the photoresist was stripped off in a 20-min ultrasonic acetone bath followed by 20-min isopropanol rinse.

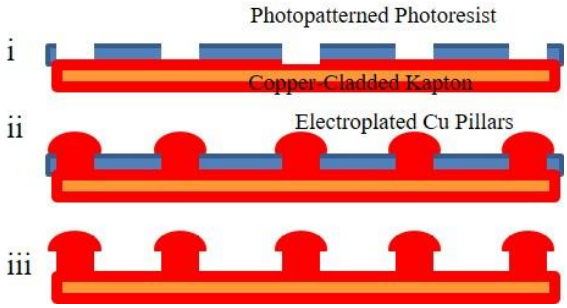

Fig.2. 4 *The process flow for fabricating copper pillars i. Spin-coat and photo-pattern photoresist, ii. Electroplate pillars through the photoresist, allowing an over-plating to reach the desired thickness iii. Copper pillars after removal.*

The copper micro pillars employed as the flow paths in hybrid wicking structures were obtained through a same photo-patterning process as that for vapor pillars. But instead of electroplating, copper micro pillars of wicking structures were fabricated

by wet etching due to the narrower spacing between micro pillars, leading to challenges in electroplating.

2.3.2 Bonding of Stainless Steel Mesh to Copper Micro Pillars

The bonding between stainless steel mesh and copper micro pillars was achieved by electroplating. Stainless steel mesh was first cleaned with ultrasonic acetone bath and isopropanol bath to remove the organic residues, then cleaned with 10 wt.% sulfuric acid solution and rinse with deionized water. The bonding fixture was assembled as shown in Fig. 2.5, a 3-mm thick rubber sheet was placed onto a 5-mm thick acrylic plate, micro pillars samples with areas without pillars protected by blue tape was then placed onto rubber sheet, then the stainless steel woven mesh was added onto micro pillars with stainless steel mesh slightly larger than the pillars area, then a 1-mm thick nylon mesh was added, followed by a 5-mm thick acrylic plate with 4-mm circular opening to allow electrolytes flowing freely to the stainless steel mesh and copper pillars, while providing clamping force to promote bonding quality. After all pieces were stacked together, they were placed in between several acrylic square frames with nylon screws. It was found that electroplating under high current density ($0.04A/cm^2$), 10 times of the current density used for electroplating vapor pillars, rendered the best bonding quality. So the sample was plated at 2.0 A for 15 min. After electroplating, the hybrid wicking structure sample was cleaned in

three progressively-cleaner deionized water baths, each lasting for 15 min. The excess area of stainless steel mesh was subsequently cut out.

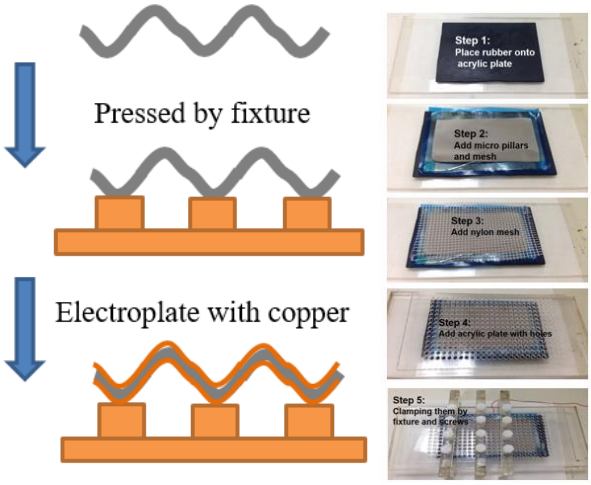

Fig.2. 5 *The process of bonding stainless-steel mesh onto copper micro pillars*

2.3.4 Assembly of TGPs

After wicking structure sample and vapor core sample were prepared, they were cleaned in acetone and isopropanol bath with ultrasonic agitation, each lasting for 20 min. Both samples were pre-tinned around the perimeter with a 10 μm thick and 5 mm wide SnPb (60/40) solder, using an HCl-based liquid solder flux. The two layers were then cleaned with ultrasonication in acetone and isopropanol for 5 min each, and then exposed to oxygen plasma with a power of 75 W at 1 Torr for 5 min to form a hydrophilic surface. The three sides of the perimeter were soldered together in an initial flux-free solder step to form a mechanical joint, using a thermos-pressing tool that applied 100 psi of pressure while locally heating the solder bond to 300 °C.

This was followed by a second solder step using flux to seal any micro-cracks in the first soldering step. This necessarily over-coated the solder, giving a final solder thickness of 150 μm. At this thickness, the solder can be bent with a 2.5 mm radius without exceeding the 3% relative elongation limit. Then a 3 cm long, 1mm outer-diameter copper tube was inserted and soldered to the final side of the perimeter between the top and bottom cladding layers, to facilitate evacuation and water-charging. The tube and soldered joints were roughly 10 mm away from the active area of the TGP.

The assembled device contained a cavity, which was subsequently evacuated with a turbo-molecular pump until the pump read a pressure of 1.0×10^{-6} Torr. Due to the small diameter of the connecting tube, the pressure inside the TGP cavity could be higher, in the mTorr range, but low enough to ensure that residual non-condensable gases only made up < 0.1% of the vapor after water charging. After evacuation, the device was charged with de-gassed and de-ionized water at a volume of 0.34 mL. The amount of water was experimentally determined to be optimal by the following method: starting with 0.15 mL of water, then increasing the applied power to 3.0 W, and slowly increasing the amount by increment of 0.025 mL until the change of thermal resistance was less than 10 %, then changing the increment to 0.005 mL until a slight increase of thermal resistance was observed.

2.4 Testing System and Data Reduction

The thermal performance testing apparatus of ultra-thin TGPs is shown in Fig 2.6. The heat was applied to the TGP with an 8 mm × 8 mm ceramic heater mounted to a 1-mm thick larger copper block with a size of 8 mm × 50 mm, matching the width of the TGP active areas under testing. The area of the TGP evaporator was defined by the size of the copper block providing heat input. Applied heat load was determined by the I-V power applied to the ceramic heater. The instrumental uncertainty in the heating power is 0.01 W. heat was removed from the TGP through the aluminum condenser block as shown in Fig 2.6. Here, the area of the condenser block was determined by the size of a 1-mm thick copper heat spreader on top of the aluminum condenser block, which was kept at the same width of the width of TGPs' active area, and the length was 25 mm. Matching the width of the evaporator and condenser with the TGP allowed us to consider the TGP as a one-dimensional heat transfer device.

The aluminum condenser block contained a region with a linear array of thermocouples and a constant 1 cm × 1 cm cross-section, which could be used to determine the heat traveling through the condenser according to Fourier's law. The base of the condenser block was maintained at a controlled temperature by a chiller system. The TGPs, heat spreaders, heater, and condenser block were all thermally connected with conductive thermal paste with a thickness of 50 ~ 75 μm and mechanical clamping with pressures in the range of 15 – 25 psi. This pressure was determined by increasing the clamping pressure did not further change the measured thermal resistance during an initial test. To verify that variations in interfacial

thermal resistance do not significantly affect the results, a TGP sample was mounted, tested, and removed from the test fixture three times, with evaporator and condenser temperatures shown good repeatability. The temperature difference between the evaporator and condenser temperatures varied by less than 3 % between the tests. During testing, the device was shrouded in fiberglass insulation to minimize convective parasitic heat losses, the ratio of output heat to input heat was typically 67 % due to the parasitic loss. The thermal resistance of TGP was defined by the ratio of the difference of the average temperature between the evaporator region (heating area) and the condenser area, to the heat flow out of the device through the condenser.

The output power was calculated by the Fourier's Law:

$$Q_{out} = k_{Al} A_{Al} \frac{T_a - T_b}{\Delta x} \tag{2.1}$$

And the thermal resistance was defined as:

$$R = \frac{T_{evap} - T_{cond}}{Q_{out}} \tag{2.2}$$

The effective thermal conductivity was defined as:

$$k_{TGP} = k_{Cu} \frac{R_{Cu}}{R_{TGP}} \tag{2.3}$$

The uncertainty was analyzed by standard error propagation:

$$\sigma_{Q_{out}} = k_{Al} \left[\sigma_{A_{Al}} \frac{T_a - T_b}{\Delta x} + A_{Al} \frac{\sigma_{(T_a - T_b)}}{\Delta x} + A_{Al} \frac{(T_a - T_b)\sigma_x}{(\Delta x)^2} \right] \tag{2.4}$$

$$\sigma_R = \frac{\sigma_{(T_{evap} - T_{cond})}}{Q_{out}} + \frac{(T_{evap} - T_{cond})\sigma_{Q_{out}}}{{Q_{out}}^2} \tag{2.5}$$

$$\sigma_{k_{TGP}} = k_{Cu} \left(\frac{R_{Cu}\sigma_{R_{TGP}}}{R_{TGP}^2} + \frac{\sigma_{R_{Cu}}}{R_{TGP}} \right) \tag{2.6}$$

The uncertainty of the K-type thermocouples is ± 0.2 °C. The uncertainty of measurement of thermocouples location is ± 0.5 mm, which is the diameter of thermocouples' holes.

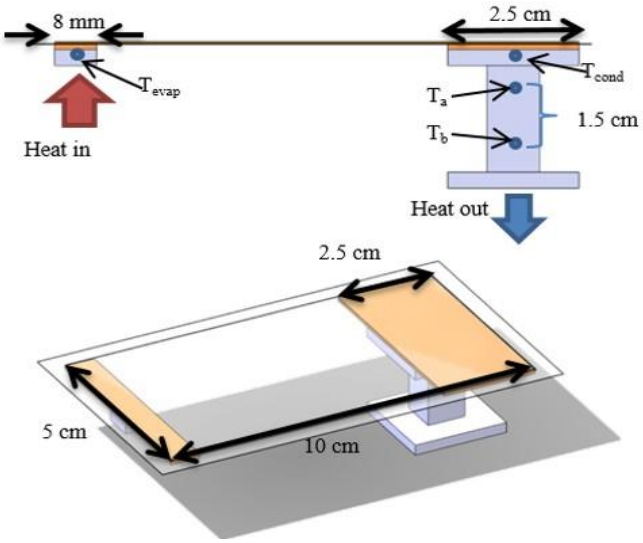

Fig.2. 6 *The side-view and the isometric-view of test setup for ultra-thin TGPs*

2.5 Results and Discussion

The thermal performance of five ultra-thin TGP prototypes is plotted in Fig. 2.7. Here a reference copper heat spreader at a size of 10 cm × 5 cm × 0.031 mm was also tested using the same test setup, which gave an average thermal resistance value of 15.3 K/W and was also plotted as the black square curve in Fig. 2.7(a), and the blue dashed line showed the theoretical value of the copper reference, which was estimated to be 16.1 K/W. The deviation of the measured and theoretical thermal resistance of copper reference was smaller than 5%.

As the applied power increased, the thermal resistance of TGPs gradually reduced due to enhanced evaporation heat transfer. As applied power was smaller than 5W, the measured thermal resistance of five TGPs varied from one another, which could be potentially caused by the different amount of non-condensable gases existing inside the TGPs prototypes. As the applied power increased, the vapor saturation temperature elevated, leading to a smaller pressure drop in the vapor space. Additionally, although there existed a different amount of non-condensable gases, whose effect on the thermal performance became negligible as the vapor volume increased. As a result, the thermal resistance of five ultra-thin TGPs was similar except TGP_S5 when applied power is greater than 5 W. It was found that TGP_S5 had a relatively thicker vapor core due to more over-plated vapor pillars, leading to reduced vapor pressure drop. This also contributed to a higher capillary limit for TGP_S5, which dried out when the applied power became greater than 10.5W, compared to 8 ~9.5 W for the other four TGPs.

With all the tested power, the effective thermal conductivity of five ultra-thin TGPs was higher than a copper reference. And the maximum effective thermal conductivity of the best-performed ultra-thin TGP was around 2600 W/m-K at an applied power of 10.5 W, greater than six times that of a copper reference. The maximum effective thermal conductivity of all ultra-thin TGP prototypes exceeded 1200 W/m-K, three times that of a coper reference.

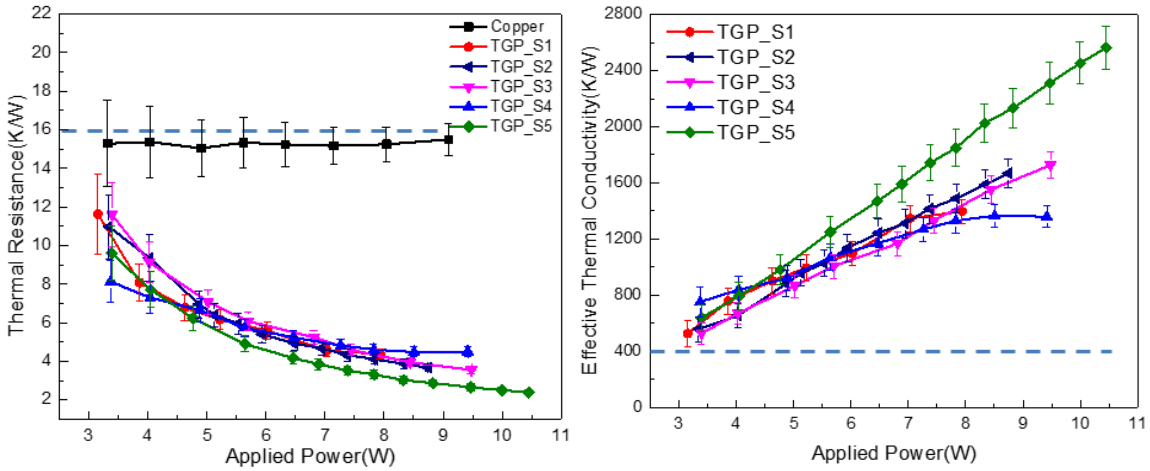

(a) *(b)*

Fig. 2. 7 *The thermal performance of ultra-thin TGPs (a) Thermal resistance as a function of applied power (b) Effective thermal conductivity as a function of power*

The thermal performance of three ultra-thin TGP prototypes operating under different condenser temperatures was studied by varying the temperature of the chiller, which was set at 12 °C and 22 °C, respectively. The results are plotted in Fig. 2.8. Under both set temperature of the chiller, the thermal resistance of ultra-thin TGPs was smaller than a copper reference, indicating a better heat spreading effect. With a cooler condenser, all the ultra-thin TGP prototypes could be tested until they reached the dryout condition due to a lower evaporator temperature compared with a warmer condenser. Additionally, for all these three TGP prototypes, the measurement was stopped when the evaporator approached 70 °C, because further increasing the power could potentially cause the pressure inside the TGP prototypes higher than the atmosphere pressure, leading to inflammation inside TGPs, which could destroy the TGP prototypes.

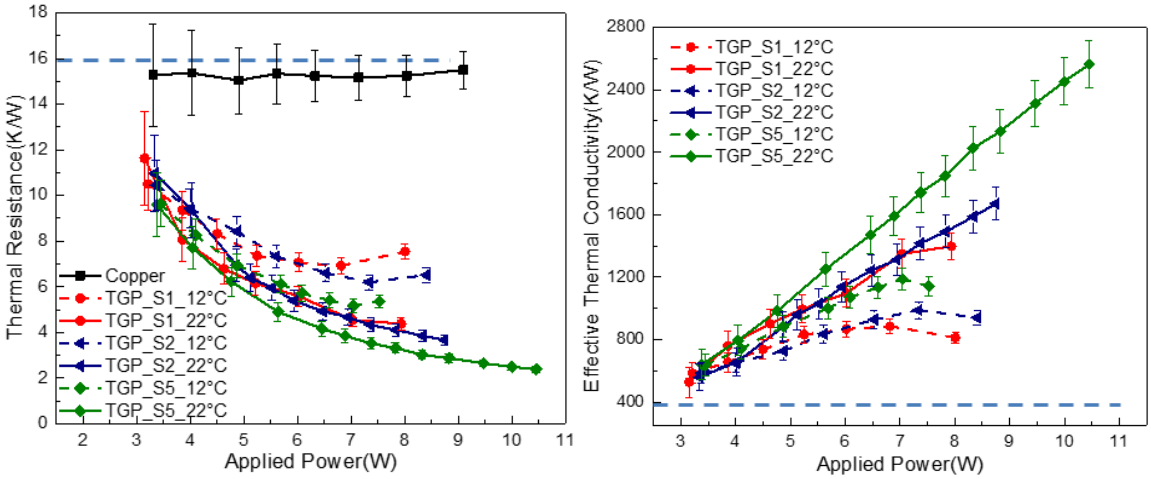

(a) (b)

Fig.2. 8 *The effect of condenser temperature on the thermal performance of ultra-thin TGPs (a) Thermal resistance as a function of applied power (b) Effective thermal conductivity as a function of applied power (solid lines are the results of TGPs operating with warmer condenser while dashed lines are the results of TGPs operating with cooler condenser)*

For these three ultra-thin TGP prototypes, operating with a warmer condenser could significantly reduce the lateral temperature difference, rendering a lower thermal resistance. Furthermore, the maximum heat load of ultra-thin TGPs was enhanced substantially when the ran with a warmer condenser. The main reason was that a warmer condenser resulted in higher saturation temperature of the vapor. This would increase the vapor density, leading to a smaller vapor-phase velocity which yielded to a reduced vapor pressure drop. So the temperature difference between the evaporator and condenser became smaller, and the capillary limit was also increased.

To test the reliability of ultra-thin TGPs, the same measurement was run 45 days after the TGP was assembled, with the chiller temperature set to 22 °C.

Compared with the performance during the first day, the difference in the thermal resistance was negligible until the applied power increased to more than 6.0 W. And at an applied power of 7.0 W, the thermal resistance increased by 18 %. The degradation can be attributed to: 1) solder slowly reacted with water and produced contaminants that gradually changed the surface from super-hydrophilic to hydrophilic; 2) non-condensable gas was generated and clogged the condenser region.

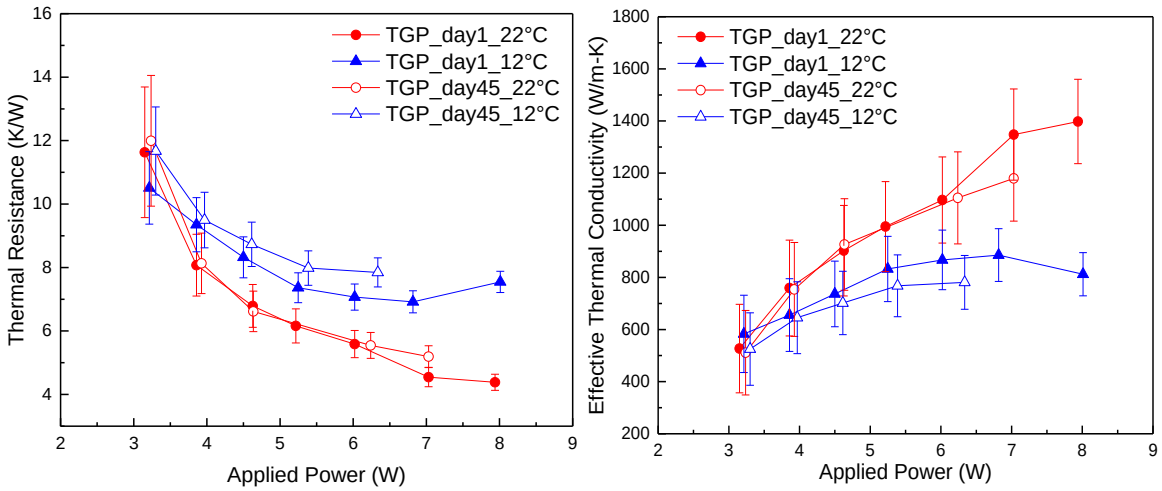

Fig.2. 9 P*erformance degradation study of TGP (a) Thermal resistance as a function of applied power (b) Effective thermal conductivity as a function of applied power*

CHAPTER 3 CAPILLARY EVAPORATION ON THIN WICKING STRUCTURES

3.1 Introduction

Capillary evaporation is the key to the thermal performance of TGPs. The onset of nucleate boiling has been shown to significantly reduce the thermal resistance and increase the dryout heat flux for capillary evaporation. Sintered powders and micro mesh are ideal for high heat flux applications since they're able to continue to supply liquid to the evaporator through the stochastically interconnected network. Sintered powders exhibit higher contact thermal resistance due to point contact between powders and the solid substrate, and the high temperature required for sintering limits their integration to electronic packages whose materials are usually polymer, furthermore, the low permeability of sintered powders results in large flow resistance. Micro-mesh wicking structures, on the other hand, have higher permeability and can be bonded via low-temperature diffusion bonding, and they are easily scalable and have low cost, and therefore this thesis study focused on studying the effects of geometric parameters including layers thickness and mesh sizes on the heat transfer performance of micro-mesh wicking

structure, during which a boiling limit was observed, the dryout heat flux didn't increased further as the number of micro mesh was increased from 4 layers to 6 layers or openings of micro mesh were varied by changing the mesh sizes due to insufficient vapor removal. Two different methods have been used to promote the capillary evaporation heat transfer performance by enhancing the vapor removal and increasing the nucleation site density: to use inline-aligned micro mesh wicking structure; and to implement nanostructured surface.

Experiments with multiple samples with thickness ranging from 148 μm (2 layers) to 413 μm (6 layers) demonstrated that at low heat flux (< 10 W/cm^2), the heat transfer coefficients of micro-mesh wicking structures showed weak dependence on the thickness, similar to findings in [62][43], as the heat flux increased, the heat transfer coefficients of thicker wicking structures were higher than thinner ones due to the onset of nucleate boiling. As the heat flux became larger than 80 W/cm^2, wicking structures with medium thickness (4 layers of 280 μm) exhibited higher heat transfer coefficient than a thicker one (6 layers of 413 μm). The experimental results have demonstrated that the 4-layer inline-aligned micro mesh wicking structure exhibited higher dryout heat flux and heat transfer coefficient than staggered-aligned structure. For 4-layer micro mesh wicking structure, the dryout heat flux was weakly dependent on the mesh sizes investigated (# 100, # 145, and # 200), while a finer mesh size yielded higher heat transfer coefficients due to increased surface area for thin film evaporation. The maximum heat flux from 4-layer # 100 micro mesh wicking structure was around 143.0 W/cm^2 for a heater of size 10 mm × 10 mm. By

implementation of nanostructured surface, the maximum heat flux of 4-layer micro mesh was increased from ~ 100 W/ cm^2 to around 190 W/cm^2.

3.2 Sample Fabrication

Micro mesh wicking structures were fabricated by diffusion bonding multilayer micro mesh onto 0.127-mm thick copper substrate under a pressure of 40 MPa at 275 °C for 12 h. Copper micro meshes were cleaned in an ultrasonic acetone bath for 15 min to remove the organic residues, and then rinsed in ultrasonic isopropanol bath for 5 min to remove acetone. Then the samples were soaked in 5wt % dilute sulfuric acid solution to remove copper oxide and thoroughly rinsed in deionized water. The micro meshes were stacked together and sandwiched between two mirror-polished stainless steel flat plates; the sandwiched structure was then clamped by two 3-in stainless steel flanges. The whole fixture was placed into the vacuum oven. The oven was evacuated to -25 psi for 5 min, then heater was turned on and the temperature was set to 275 °C, the oven was under vacuum through the whole bonding process. After 12 h at 275 °C, the sample was cooled down for more than 6 h.

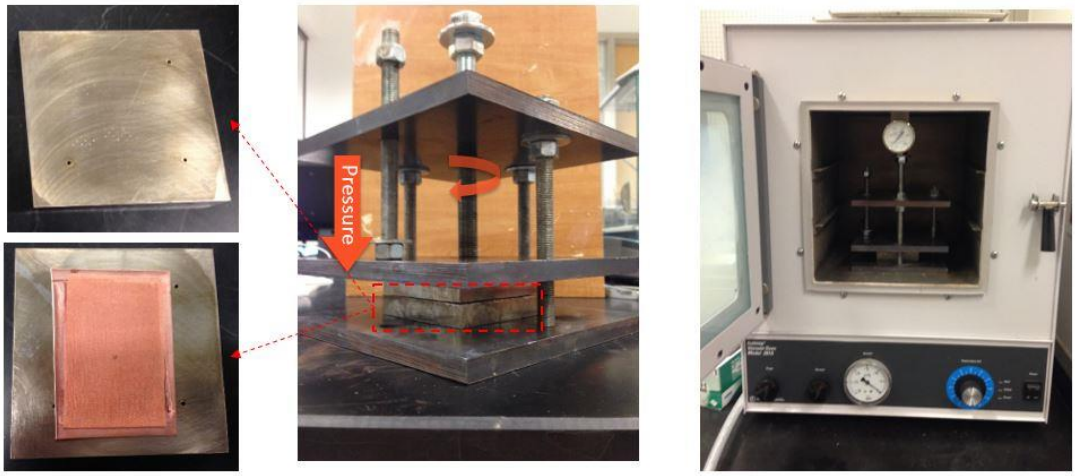

Fig. 3. 1 *The fixture and vacuum oven for low-temperature diffusion bonding*

Different samples were fabricated with three different layer thicknesses (2 layers, 4 layers, and 6 layers), two different alignments including inline stacking and staggered stacking, and three different mesh sizes (# 100, # 145, and # 200). For all the wicking structure samples, the porosity was maintained constant, approximately 0.50, except that # 200 micro mesh had a porosity of 0.60. Additional samples of # 200 micro mesh were used for studying the effect of nanostructures.

3.3 Rate of Rise Test Setup and Data Reduction

The maximum heat flux of TGPs is most frequently determined by the capillary performance of their wicking structures. The capillary rate of rise experiments have been used to assess the capillary performance of micro mesh wicking structures. As shown in Fig. 3.2, a micro mesh sample with 13 mm × 25 mm was mounted perpendicular to the horizontal surface of a liquid reservoir, and the liquid was slowly

added into the chamber until the meniscus started to contact with the bottom of the micro mesh sample.

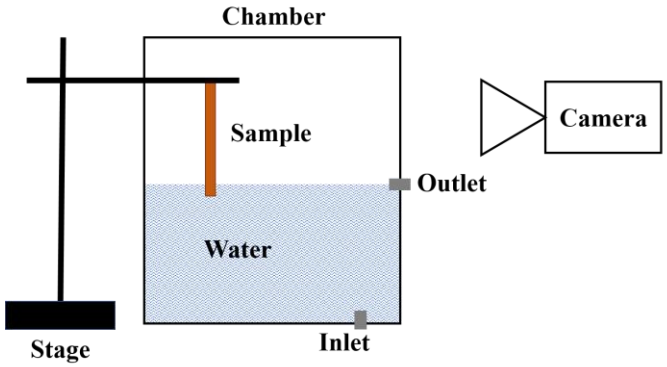

Fig. 3. 2 *The experimental test setup for the capillary rate-of-rise measurement*

The liquid then rised along the microporous structure and imaged using an iPhone 7 plus device, and the liquid front was tracked using iPhone 7 plus camera operating at 60 frames per second. Filtered deionized water was used as the test fluid here since it was the working fluid for the capillary evaporation experiments. The experiment was conducted inside a chamber with atmosphere saturated with water vapor to minimize the evaporation effects, and by neglecting the evaporation effects, with the following assumptions: (i) the flow is one-dimensional (ii) no inertia or entry effects in the liquid reservoir (iii) no friction or inertia effects by displaced air occur (iv) the viscous pressure loss inside the micro mesh is given by Darcy's Law, the liquid rise was therefore controlled by viscous, gravitational, and capillary effects [98]:

$$t = -\frac{h}{b} - \frac{a}{b^2}\ln\left(1 - \frac{bh}{a}\right) \tag{3.1}$$

where $a = \frac{1}{\mu}\frac{2\sigma cos\theta}{R}\frac{K}{\varepsilon}$ and $b = \frac{\rho g}{\varepsilon\mu}K$

As shown in Fig. 3.3(a), the fluid flow was one dimensional, and Fig. 3.3 (b) shows a representative data of measured rise height versus time; a non-linear regression was performed in Matlab to extract a and b to get permeability and capillary pressure.

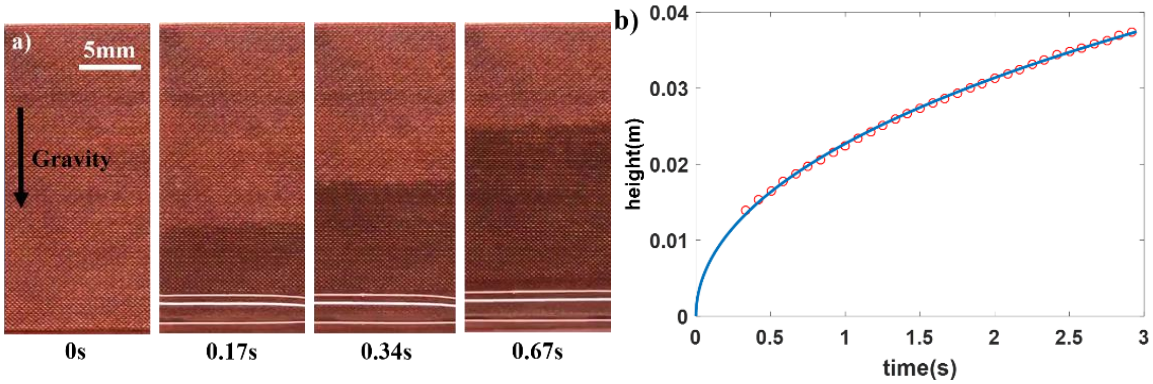

(a) *(b)*

Fig. 3. 3 *(a) Example image sequence from capillary rate of rise experiment on 4-layer # 200 micro mesh wicking structure (b) Representative data of measured liquid front height versus time and non-linear regression of the data to extract a and b to obtain permeability and capillary pressure of micro mesh wicking structures*

Let $\vec{P} = (a, b)$, and h_i be the fitted value for $t = t_i$, then the differential between fitted and measured value can be expressed as $w(\vec{P}) = \sum_i \{h_i - f(t_i, \vec{P})\}^2$, at best fit of $f_i + \vec{P}$, $\nabla_P w = \vec{0}$. That is

$$\sum_i \left[h_i - f\left(t_i, \vec{P}^0\right) \right] \frac{\partial f}{\partial P_l} = 0 \text{ for } \forall P_l \in \vec{P}^0 \tag{3.2}$$

The first order of Taylor expansion of $f(t_i, \overrightarrow{P^*})$:

$$f\left(t_i, \vec{P}^*\right) = f\left(t_i, \vec{P}^0\right) + \sum_l \frac{\partial f\left(t_i, \vec{P}^0\right)}{\partial P_l} \left(P_l^* - P^0\right) \tag{3.3}$$

Combining equations (3.2) and (3.3)

$$\sum_i \left[h_i - f\left(t_i, \vec{P}^*\right) - \sum_l \frac{\partial f\left(t_i, \vec{P}^0\right)}{\partial P_l}\left(P_l^* - P^0\right) \right] \frac{\partial f}{\partial P_l} = 0 \tag{3.4}$$

This can be written as

$$J_P^T \left(\vec{H} - \vec{F}(\vec{P}^*) - J_P \left(\vec{P}^* - \vec{P}^0 \right) \right) = 0 \tag{3.5}$$

where $\underset{H}{\rightarrow} = (h_1, h_2, \ldots, h_n)^T$, $\underset{P}{\rightarrow} = (p_1, p_2)^T$ and the Jacobian matrices

$$J_P = \begin{pmatrix} \frac{\partial f}{\partial p_1}(t_1) & \frac{\partial f}{\partial p_2}(t_1) \\ \vdots & \vdots \\ \frac{\partial f}{\partial p_1}(t_n) & \frac{\partial f}{\partial p_2}(t_n) \end{pmatrix} \tag{3.6}$$

So that

$$\vec{P}^* - \vec{P}^0 = \left(J_P^T J_P \right)^{-1} J_P^T \left(\vec{H} - \vec{F}(\vec{P}^*) \right) \tag{3.7}$$

And the variance of fitted parameters:

$$\begin{aligned} \operatorname{var}(\vec{P}^* - \vec{P}^0) &= \begin{pmatrix} \sigma_{p_1}^2 & \operatorname{cov}(p_1, p_2) \\ \operatorname{cov}(p_1, p_2) & \sigma_{p_2}^2 \end{pmatrix} \\ &= \left(J_P^T J_P \right)^{-1} J_P^T \operatorname{var}\left(\vec{H} - \vec{F}(\vec{P}^*) \right) J_P \left(J_P^T J_P \right)^{-1} \end{aligned} \tag{3.8}$$

3.4 Capillary Evaporation Test Setup and Data Reduction

A test facility has been developed to simulate the internal conditions of the evaporator region in an operating TGP and supply the working fluid (water in this

study) to the micro mesh wicking structure in the same way as that occurs within an actual TGP. The subsections below describe the test setup and the data reduction.

3.4.1 Capillary Evaporation Test Facility

A test facility has been developed to conduct capillary evaporation heat transfer studies. The schematic of the experimental system for capillary evaporation measurement is shown in Fig. 3.4. The test chamber provided a saturated environment into which the sample dissipated heat and allowed for capillary evaporation. The diameter of the stainless-steel vacuum chamber was 152.4mm and it was 76.2mm deep, with one side of the chamber containing a quartz glass with a diameter of 101.6 mm as a visualization window, and the other side was designed for the sample installation. The inside of the chamber was coated with Al_2O_3 and TiO_2 via atomic layer deposition method (Beneq TFS ALD reactor) to prevent corrosion. External lightning was provided for visualization studies. One cartridge heater was mounted at the bottom of the chamber to assure saturated working conditions. A PID temperature controller (Infinity fluids corporation) was used to accurately control the water temperature. Highly purified water was degassed by boiling for more than two hours right before tests. A built-in compact condenser was designed to keep a constant water level by timely recycling the condensate. The vapor pressure and temperature inside the chamber were monitored by a pressure gauge and one T-type thermocouple, respectively. All tests were conducted with samples positioned in the

vertical direction. The fluid flow and bubble dynamics were captured by a high-speed camera (Photron FASTCAM SA4).

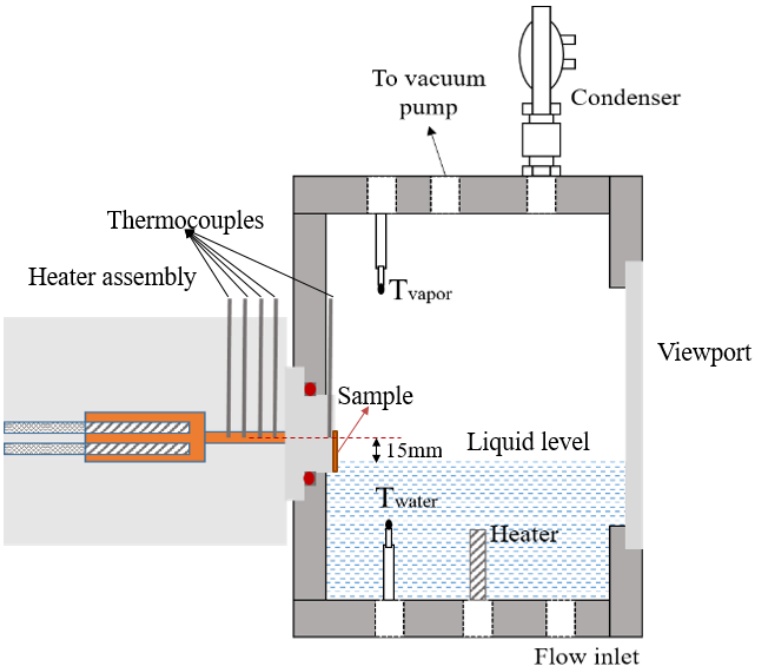

Fig. 3. 4 *The schematic of the test facility for capillary evaporation measurement*

The heater assembly is shown in Fig. 3.5. The heat input was generated by four 250W, ¼" Omega cartridge heaters embedded into the back end of a copper square rod with cross-section of diameter of 31.75 mm, this cross-section was then reduced to 10 mm × 10 mm over a 57.15 mm length through which the heat flux was concentrated and conducted to the back of the sample, four K-type thermocouples were inserted into 0.51 mm diameter holes manufactured into the tip. The last thermocouple was 1 mm away from the tip. The heat flow in this tip was observed from the thermocouple measurements to be constant for all the tests. The measured, linear temperature gradient can thus be used to calculate the supplied heat flux as

well as to estimate the substrate temperature by extrapolation. The entire copper block was insulated with 76.2 mm diameter of Macor ceramic (k = 1.46 W/m·K) on all sides, which was further encapsulated in high-temperature fiberglass insulation. The interface between the copper block and Macor ceramic was sealed by high-temperature silicone (Loctite silicone sealant).

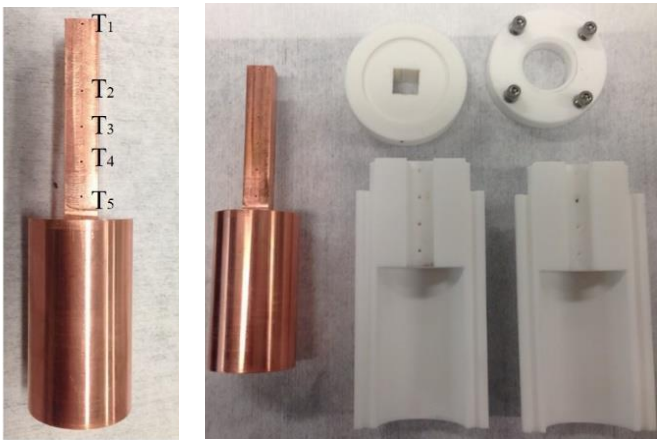

Fig. 3. 5 *The copper heating block and the high-temperature ceramic insulator*

3.4.2 Capillary Evaporation Test Procedures

Each sample was attached to the heater block by soldering with significantly higher thermal conductivity compared with thermal greases, pads and other standard interface materials. The higher conductivity and the well-defined and minimized thickness of this interface were critical for reducing the uncertainty in estimating the temperature drop across this interface. A thin layer of 100 μm thick solder paste was applied evenly onto the copper tip, after heating the solder paste to 175 °C, the test sample was placed onto the heater, and letting the sample surface to

heat for around 3 min to oxidize to prevent solder flowing into the micro mesh. Then a copper block of 520g, with the same area of the ceramic insulator, was placed onto the sample to apply pressure for enhancing the soldering quality.

Immediately before insertion into the test facility, all soldered samples were treated to remove any organic contaminants or minor non-uniform surface oxidation that might have occurred. The samples were dipped in acetone and thoroughly rinsed with deionized water to remove any grease. The samples were subsequently immersed in a dilute acid piranha solution and rinsed with deionized water to strip the surface of contaminants and oxide layer. Then the samples were cleaned in an oxygen plasma at 80 W for 5 min to form a superhydrophilic surface.

At the beginning of each test, the sample was sealed into the test facility, and the chamber was filled with high purity water which was pre-degassed by vigorously boiling for 2 h. The chamber was then evacuated by a vacuum pump to remove the non-condensable gas and oxygen. The water was kept at the saturation temperature of 94 °C (Boulder). And the water level was set to be 15 mm down from the center of the heater.

Before the recording of any test data, the test facility was allowed to reach steady state, defined as the point at which the temperature changed at a rate of less than 0.1 °C over a period of 10 min. The steady-state experimental data were averaged over a period of 3 min and recorded for each power level, and then the voltage was incremented and the process repeated until the wicking structure reached the complete dryout condition.

3.4.3 Data Reduction

The recorded temperatures were averaged over the final 100 data points (3 min) of the acquired steady-state data. Assuming one-dimensional heat conduction in the copper heater, the heat flux, the superheat, and the evaporation heat transfer coefficient were calculated from Eqs. (3.9) ~ (3.11), respectively:

$$q'' = \frac{1}{3} k_{Cu} \left(\frac{T_1 - T_3}{\Delta x_1} + \frac{T_2 - T_4}{\Delta x_1} + \frac{T_4 - T_5}{\Delta x_2} \right) \tag{3.9}$$

$$T_w - T_{sat} = T_5 - q'' \left(\frac{\Delta x_3}{k_{Cu}} + \frac{\Delta x_s}{k_s} \right) - T_{sat} \tag{3.10}$$

$$h_{eff} = \frac{q''}{T_w - T_{sat}} \tag{3.11}$$

The heat flux represented only the heat being transported directly through the copper block and out from its tip, and accounted for all the heat losses through the heater block insulation concerning the electrical power input. Using the measured tip temperature, T_5, and the known thermal conductivity, k_{Cu}, the temperature at the bottom of the capillary wicking structure, T_w could be derived. The effective heat transfer coefficient could be estimated by using Eq. (3.11) with these two values.

Based on the error propagation, the uncertainty of heat flux, superheat, and effective heat transfer coefficient was determined by Eqs. (3.12) ~ (3.14):

$$\sigma\left(q^{"}\right)=\frac{1}{3}k_{Cu}\left\{\begin{array}{l}\dfrac{T_4+T_3-T_2-T_1}{\left(\Delta x_1\right)^2}\sigma\left(\Delta x_1\right)+\dfrac{T_5-T_4}{\left(\Delta x_2\right)^2}\sigma\left(\Delta x_2\right)+\ldots \\ \ldots\dfrac{1}{\Delta x_1}\left[\sigma\left(T_4\right)+\sigma\left(T_3\right)+\sigma\left(T_2\right)+\sigma\left(T_1\right)\right]+\ldots \\ \ldots\dfrac{1}{\Delta x_2}\left[\sigma\left(T_4\right)+\sigma\left(T_5\right)\right]\end{array}\right\} \tag{3.12}$$

$$\sigma\left(T_w-T_{sat}\right)=\sigma\left(T_5\right)+\sigma\left(q^{"}\right)\left(\frac{\Delta x_3}{k_{Cu}}+\frac{\Delta x_s}{k_s}\right)+q^{"}\left(\frac{\sigma\left(\Delta x_3\right)}{k_{Cu}}+\frac{\sigma\left(\Delta x_2\right)}{k_s}\right)+\sigma\left(T_{sat}\right) \tag{3.13}$$

$$\sigma\left(h_{eff}\right)=\frac{1}{T_w-T_{sat}}\sigma(q^{"})+\frac{q^{"}\left[\sigma\left(T_w\right)+\sigma\left(T_{sat}\right)\right]}{\left(T_w-T_{sat}\right)^2} \tag{3.14}$$

The uncertainties of the temperature measurements, and the measurement of the length (or width) were ± 0.2 °C, 0.5 mm, respectively. The length measurement uncertainty was estimated by the diameter of the holes for thermocouple insertion. The solder joint thickness uncertainty was determined to be ± 0.025 mm. Fig. 3.6 showes a typical relation between the temperature differences and the heat flux of one of the sample tested, the heat flow was considered as constant, and the temperature distribution was linear, the variation of heat flux along the heater was less than 5% when the heat flux became greater than 20 W/cm^2.

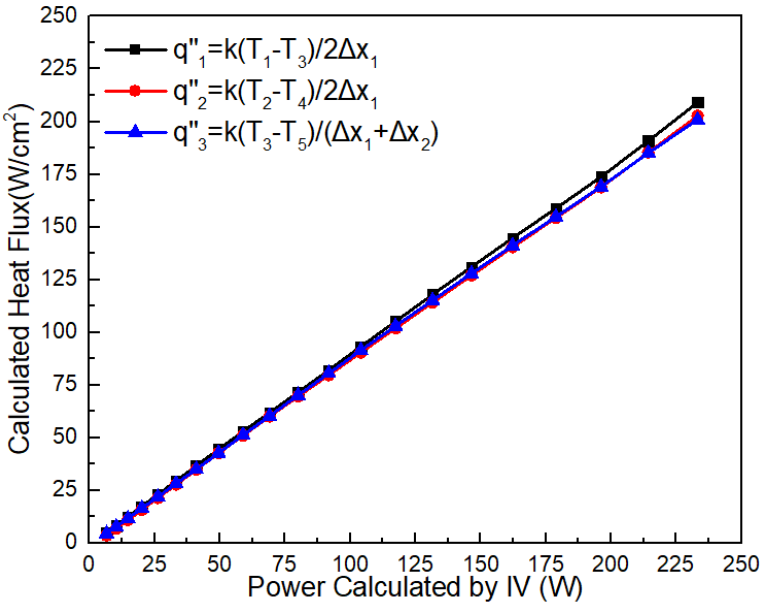

Fig. 3. 6 *A typical relation between the temperature differences and the heat flux of the surface of a 4-layer # 200 copper micro mesh wicking structure (x-axis is the power calculated by multiplying the current and voltage from the DC power supply, and y-axis is the heat flux calculated from the temperature distribution through the heating copper block)*

3.5 Results and Discussion

Test results for the micro mesh wicking structures were presented in the form of heat flux as a function of superheat, the heat transfer coefficient with input heat flux, and permeability of capillary force for different samples. A representative plot of heat transfer performance data for a 4-layer # 100 copper micro mesh wicking structure is shown in Fig 3.7. Each data point on these curves represented a steady-state measurement at the given heat flux. The dryout condition referred to a dramatic

and continuous increasing evaporator temperature accompanied by a decrease in the applied heat flux.

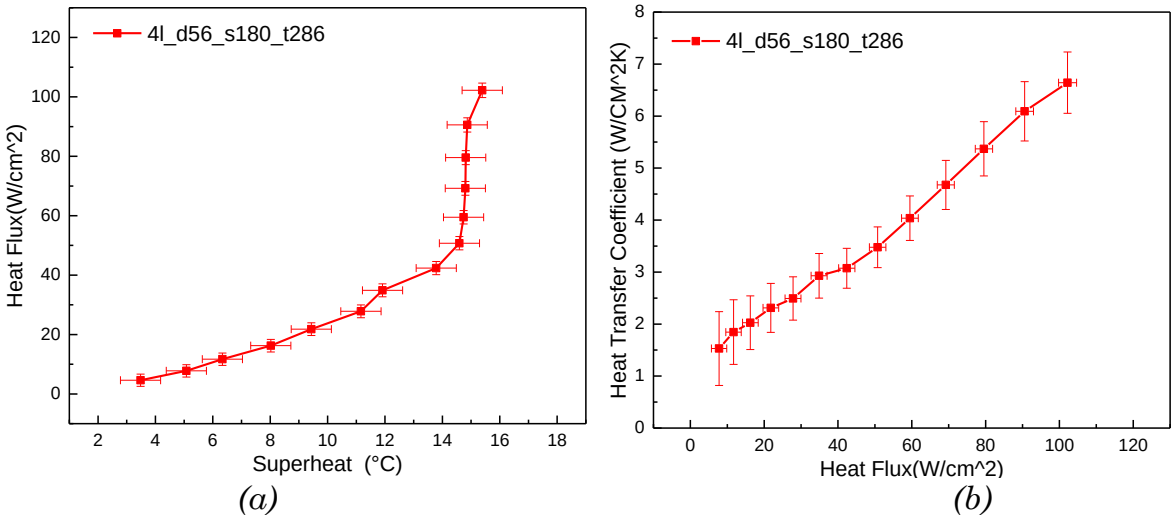

Fig. 3. 7 *Representative data of steady-state thermal performance results for 4-layer copper micro mesh wicking structure. The results are presented in the form of (a) heat flux as a function of superheat and (b) calculated sample heat transfer coefficient as a function of heat flux*

3.5.1 The Effect of Layers Thickness

The dryout heat flux of capillary evaporation is most frequently governed by the capillary limit. As the thickness of wicking structures increases, the enlarged cross-sectional area for liquid flow could dramatically reduce the flow resistance, leading to a higher dryout heat flux. However, as the wicking structures become thicker, the conduction thermal resistance through the wicking structure saturated with working fluid also becomes larger, leading to a smaller heat transfer coefficient.

As is shown in Fig. 3.8, the evaporating meniscus can be divided into three hypothetical regions [99]. Region I is the absorbed film region that has a uniform thickness, liquid in this region "cannot evaporate due to the combined effects of attractive forces between the solid and the liquid, vapor pressure, and substrate temperature. Region II is the transition region where the attractive forces of the solid are much weaker, and the liquid-vapor interface has measurable curvature. During active evaporation, the gradient in the thickness and the curvature of the liquid-vapor interface drives the flow of liquid towards this region via capillary and intermolecular forces." Region III is the bulk fluid or meniscus region where the curvature of the interface becomes nearly constant, acting as a liquid reservoir that supplies liquid to the transition region. Fig. 3.8(b) shows an idealized sketch of the thermal resistance network of a micro mesh wicking structure. R_{sub} is the substrate thermal resistance on which the micro mesh is bonded, R_{matrix} is the effective thermal resistance of the mesh/liquid (water) matrix, $R_{film}$is the thermal resistance of the thin liquid film that forms at the meniscus, and R_{in} is the thermal resistance of the liquid/vapor interface. T_{sub}, T_{wall} , T_{vap} are the temperature at the base of the substrate, temperature at the wall in contact with the liquid, and vapor temperature respectively. The thermal resistance R_{sub} induced by conduction through the solid substrate is generally small due to the high thermal conductivity of copper; R_{in} is also not the dominant resistance in such a system[4], and therefore the overall thermal resistance is dominated by the conduction through the mesh/liquid matrix and the evaporation at the thin film. As the wicking structures become thicker, the liquid film thickness also increases,

leading to greater R_{matrix} thermal resistance, so the heat will accumulate at the wall (substrate), as the heat flux increases, the superheat can be large enough to trigger nucleate boiling, which has been demonstrated to decrease the overall thermal resistance [43][56][44].

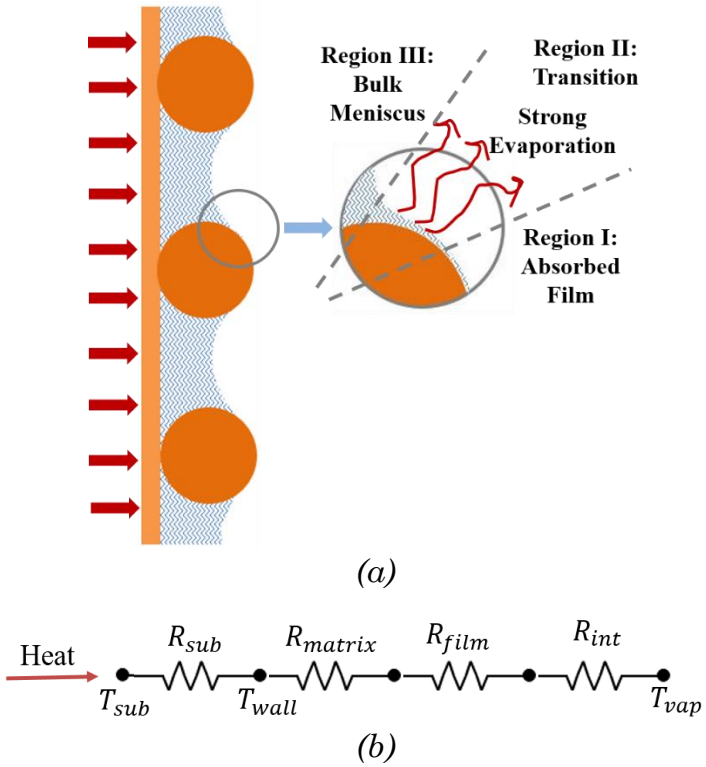

Fig. 3. 8 *Schematic of capillary evaporation on micro mesh wicking structure (a) Evaporation on micro mesh and evaporation meniscus (b) thermal resistance network*

As shown in Fig. 3.9, the onset of nucleate boiling extends the contact lines of vapor, liquid, and solid, increasing the surface areas for thin film evaporation, and thus improving the heat transfer performance by reducing the thin film evaporation thermal resistance. However, a further increase in the thickness will result in the entrapment of vapor bubbles inside the micro mesh wicking structures, which will significantly increase the thermal resistance of the mesh/liquid matrix since vapor

has a much higher thermal resistance, moreover, the entrapment of vapor also interferes with the supply of liquid to the evaporator region. It's therefore of crucial importance to investigate the effect of the thickness of micro mesh wicking structure on its heat transfer performance. Current work studied the heat transfer performance of micro mesh wicking structure with different thickness by changing the number of layers. Details of the samples are summarized in Table 3.2.

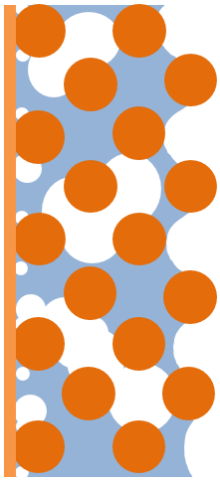

Fig. 3.9 *Schematic of nucleate boiling in micro mesh wicking structure*

Table 3. 1 *List of the micro mesh samples tested and their geometric properties*

Sample	Wire diameter	Spacing	Thickness	Porosity
2l_d56_s180_t148	56 μm	180 μm	148 μm	0.541
4l_d56_s180_t286	56 μm	180 μm	286 μm	0.522
6l_d56_s180_t413	56 μm	180 μm	413 μm	0.503

The permeability and capillary pressure of micro mesh with different thickness are presented in Fig. 3.10, 2-layer micro mesh had similar permeability with 4-layer

micro mesh, while 6-layer mesh had a relatively lower permeability, but higher capillary pressure.

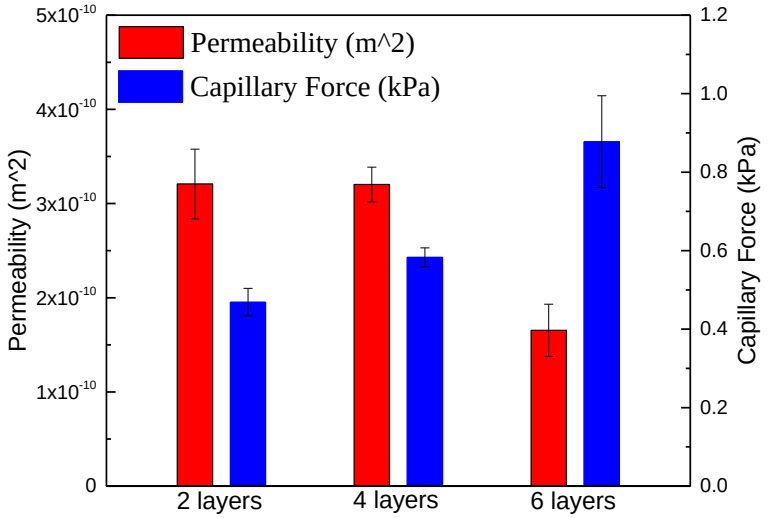

Fig.3.10 Permeability and capillary force of multilayer micro mesh wicking structures with 2 layers, 4 layers, and 6 layers (wire diameter of 56 μm, spacing of 180 μm)

The heat transfer performance of micro mesh samples is plotted in Fig. 3.11. At low to moderate heat fluxes, the heat transfer coefficient of 2-layer micro mesh increased gradually with the input heat flux. The liquid film thermal resistance was a function of thin liquid film thickness and the total length of the three-phase contact line, i.e., the total area of the thin liquid film surrounding the micro mesh wires. As long as capillary pressure provided by the micro mesh was sufficient to overcome the pressure losses during the evaporation, the fluid level would not recede into the wicking structure (towards the substrate)[43]. However, as the applied heat flux became greater than 49.3 W/cm^2, the capillary limit was reached near the top of the heater and local dryout occurred, evinced by a visible dry spot on the wicking

structure surface, a radial variation of the liquid level away from the dry spot existed, rising from zero at the edge of the spot to the top of the micro mesh wires far away from the spot, as depicted in Fig. 3.12. As a result, the effective area of the thin film was significantly enhanced, with evaporation occurring in the thin film around the micro mesh wires as well as from the substrate on which micro wires were bonded. Additionally, the contact angle was close to the minimum possible value, the receding contact angle for water on copper at high heat fluxes, this recession could potentially make the liquid film where the bulk of the evaporation occurred thinner, and slightly reduced the film thermal resistance. These two effects working in tandem improved the heat transfer coefficients at high fluxes, more obvious for heat flux greater than 49.3 W/cm^2 in 2-layer micro mesh wicking structure. Further increase in heat flux caused the dry spot to spread dramatically and eventually blanket the whole surface of the wicking structure with vapor, causing a sudden and unrecoverable temperature overshoot. In current study, 2-layer micro mesh structure dried out at 67.5 W/cm^2.

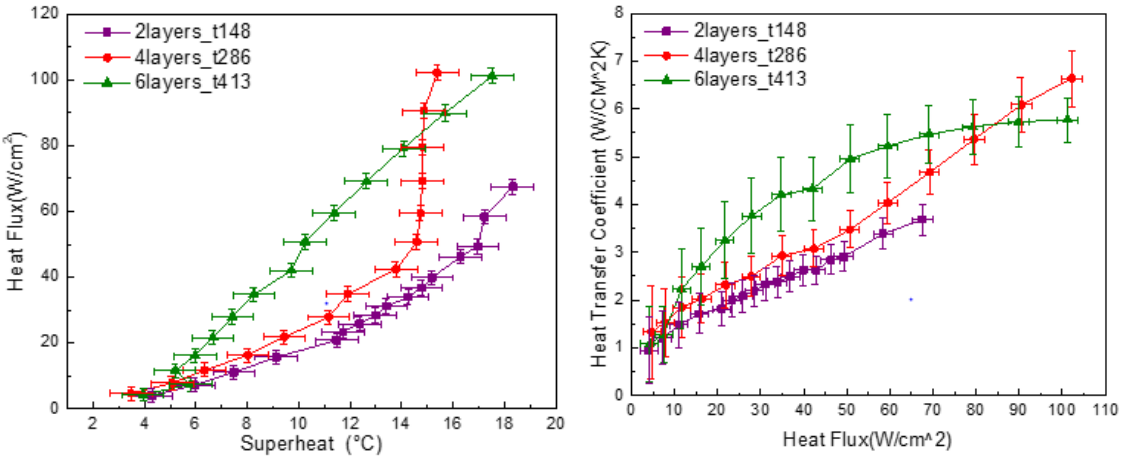

(a) *(b)*

Fig. 3.11 *The heat transfer performance of multiple layers of micro mesh wicking structures (2 layers, 4 layers, and 6 layers) (a) heat flux as a function of superheat (b) heat transfer coefficient as a function of heat flux*

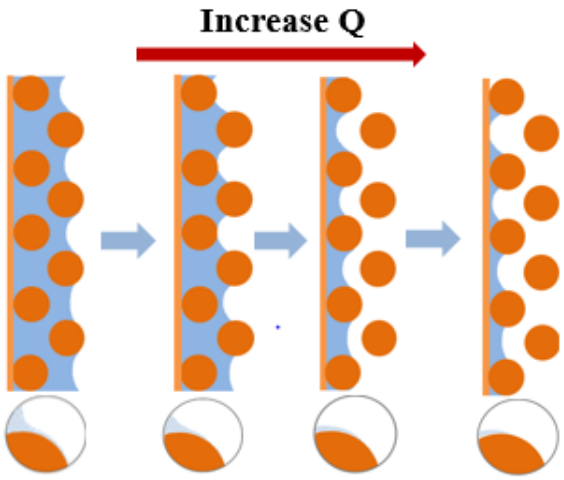

Fig. 3.12 *Sketch of the wicking structure and liquid meniscus level for 2-layer mesh*

As the wicking structure became thicker, nucleate boiling was visually observed at several locations on the micro mesh samples. There existed two distinct regions in the heat transfer curve of 4-layer micro mesh wicking structure: one corresponding to evaporation dominated region at low to moderate heat fluxes, and another corresponding to nucleate boiling dominated region at high heat fluxes. The heat transfer coefficient in the boiling regime was substantially increased due to enhanced thin film area caused by ebullition of the generated bubbles. Escaping bubbles constrained inside the micro mesh created a thin film around the micro mesh wires instead of only near the meniscus as in evaporation, yielding higher heat transfer coefficients. A steady boiling regime could be maintained until the sample dried out at 102.2 W/cm^2 beyond the nucleation incipience at 42.4 W/cm^2. And the

change of wall superheat was less than 2 °C in this region. The heat transfer regimes are depicted in Fig. 3.13.

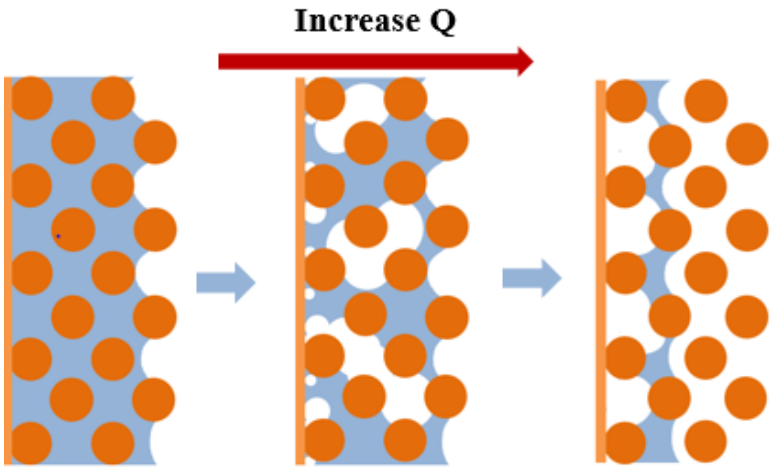

Fig. 3. 13 *Sketch of the wicking structure and liquid meniscus level for 4-layer mesh*

The superheat temperature of 6-layer micro mesh wicking structure raised nearly linearly as the heat flux was gradually incremented until 11.6 W/cm^2, during which the heat was dissipated mainly through evaporation. For the next test point of the applied heat flux, the substrate temperature was maintained for only a short time and then a sharp decrease in the superheat was suddenly observed, and the heat flux increased suddenly, indicating the onset of nucleate boiling. Following boiling incipience, during the boiling regime, the temperature steadily rised with applied heat flux but with an increased slope. The heat transfer coefficient increased with applied heat flux until it reached 68.3 W/cm^2, as heat flux further increased, the heat transfer coefficient remained nearly constant.

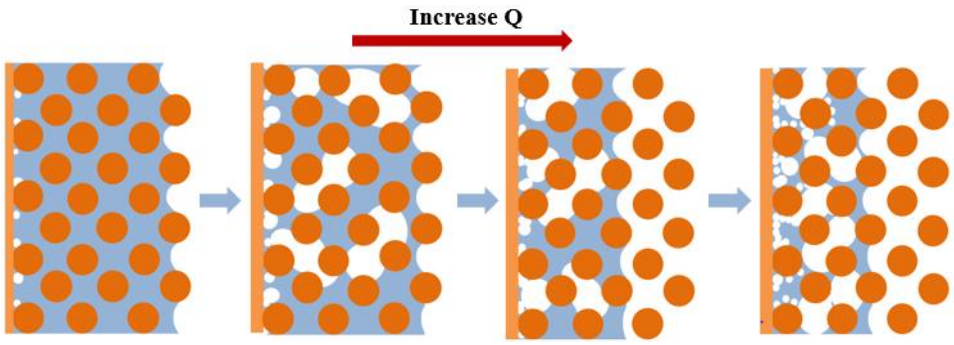

Fig. 3. 14 *Sketch of the wicking structure and liquid meniscus level for 6-layer mesh*

As depicted in Fig.3.14, the onset of nucleate boiling enhanced the heat transfer coefficients due to extended thin film regions for evaporation. As the heat flux increased and became greater than 68.3 W/cm^2, the density of nucleation site increased, however, due to the entrapped vapor bubbles inside the thicker wicking structures, these nucleate bubbles were suppressed and difficult to grow to enhance the thin film evaporation, so that the number of vapor bubbles contributing to the higher heat transfer coefficient didn't vary with further increase in applied heat flux. Moreover, the entrapped vapor bubbles also interfered with the liquid supplying to the heater area, leading to an immature dryout before it reached the capillary limit.

By comparing the heat transfer performance of all these three samples, it was clear that the heat transfer coefficient of micro mesh was independent of thickness when the heat flux was smaller than 10 W/cm^2, because the overall thermal resistance was dominated by the thin film evaporation, which was determined by the exposed surface area that was independent of wicking structure thickness when the mesh sizes remained the same[62][43]. However, the transition points of these three samples were different. First of all, nucleate boiling was absent in 2-layer micro mesh

wicking structure, the enhancement of heat transfer coefficient in 2-layer micro mesh was mainly due to extended three-phase contact line caused by liquid meniscus receding, while the heat transfer performance enhancement in 4-layer and 6-layer micro mesh wicking structure was due to the onset of nucleate boiling. However, the onset of nucleate boiling of a 6-layer micro mesh wicking structure occurred at a lower heat flux of 11.6 W/cm^2 compared with 42.4 W/cm^2. When the thickness of micro mesh increased, the mesh/water matrix thermal resistance increased, and heat tended to accumulate at the wall at lower heat fluxes compared with a thinner micro mesh, which would result in the onset of nucleate boiling occurring at a lower heat flux.

While the permeability and capillary pressure of these three samples were similar, the flow resistance of a thinner wicking structure was higher than thicker one due to the smaller cross-sectional area for liquid flow. And therefore, 4-layer micro mesh had demonstrated a higher dryout heat flux of 102.2 W/cm^2 compared with 67.5 W/cm^2 for the 2-layer micro mesh. However, a 6-layer micro mesh dried at 97.5 W/cm^2, a similar heat flux as 4-layer micro mesh, indicating that 6-layer micro mesh dried out before it reached the capillary limit, instead, a boiling limit was imposed. Vapor bubbles experienced more considerable resistance to escape at a thicker wicking structure, and therefore, vapor bubbles tended to be constrained inside the micro mesh wicking structure, explaining higher heat transfer coefficient of 6-layer micro mesh wicking structure compared with 4-layer micro mesh. Nevertheless, the entrapped vapor bubbles caused flow blockage, leading to dryout.

While increasing the thickness could increase the maximum heat flux of thin micro mesh wicking structure due to the onset of nucleate boiling, there existed an optimum thickness that gave the highest dryout heat flux, further increase in the thickness wouldn't increase the dryout heat flux due to increased resistance for vapor bubbles to escape.

3.5.2 The Effect of Mesh Sizes

Although a 6-layer micro mesh wicking structure provided a larger cross-sectional area for liquid flow compared with a 4-layer micro mesh, it didn't increase the dryout heat flux due to a boiling limit. And therefore, the efficient removal of vapor bubbles played an essential role in improving the dryout heat flux of multilayer micro mesh wicking structure. This part describes the effect of the pore sizes (mesh sizes) on the heat transfer performance of 4-layer micro mesh wicking structures: three different mesh sizes had been used in this study, # 100, # 145, and # 200.

Details of the parameters of the six tested samples are shown in Table. 3.3. The variation of wire diameter was within 10%, and the pore size of # 145 was slightly larger than that of # 200 mesh, while # 100 mesh had nearly as twice large pore size as the other two mesh sizes. Although the wire diameter was similar, the obtained micro mesh samples had different thickness, as shown in Table 3.3, # 100 mesh with the largest spacing (pore size) had the smallest thickness, while # 200 mesh with thinnest wires but the obtained samples were the thickest. This was because the

smallest spacing and twill weave of # 200 mesh worked together and made finer mesh more robust and deformed less during bonding.

Table 3.2 *List of the micro mesh samples tested and their geometric properties*

Sample	Wire diameter	Spacing	Thickness	Porosity
4l_d56_s180_t286	56 μm	180 μm	286 μm	0.522
4l_d56_s180_t280	56 μm	180 μm	280 μm	0.499
4l_d56_s100_t321	56 μm	100 μm	321 μm	0.514
4l_d56_s100_t319	56 μm	100 μm	319 μm	0.527
4l_d51_s80_t373	51 μm	80 μm	373 μm	0.615
4l_d51_s80_t358	51 μm	80 μm	358 μm	0.590

Fig. 3.15 shows the measured permeability and capillary pressure of 4-layer micro mesh wicking structures. Although the pore size of single-layer micro mesh of different mesh sizes varied a lot, the permeability and capillary pressure showed a weak dependence on the mesh sizes. First of all, both # 100 and # 145 micro mesh were plain weaved, while # 200 micro mesh was twill weaved; secondly, with similar sized micro wires, the micro mesh layers with larger openings between micro wires tended to slide from each other, reducing the effective pore sizes. These two effects worked together, leading to the small difference of the effective pore sizes of 4-layer micro mesh wicking structures with different mesh sizes, as is shown in Fig. 3.16.

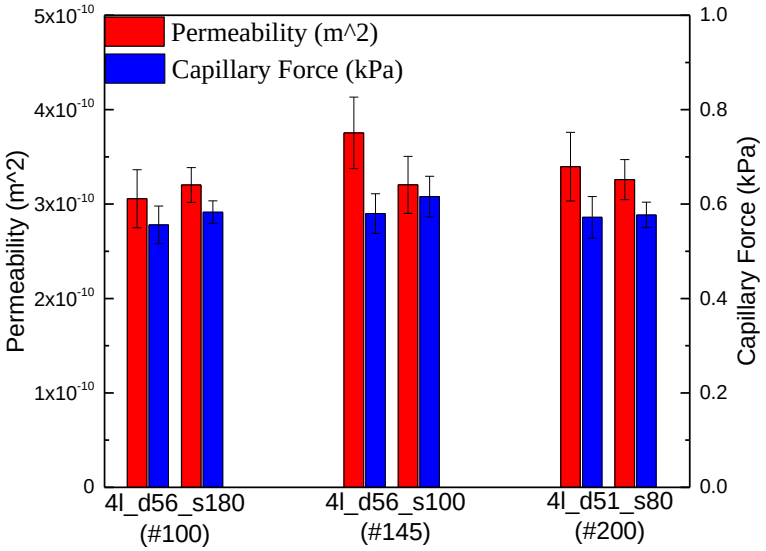

Fig. 3.15 *Permeability and capillary force of 4-layer micro mesh wicking structures of different mesh sizes (# 100, # 145, and # 200)*

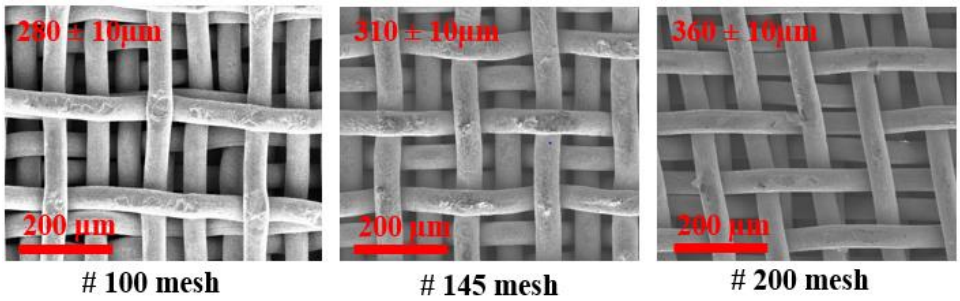

Fig. 3. 16 *SEM images of 4-layer micro mesh structures of different mesh sizes*

The heat transfer curves of these samples are plotted in Fig.3.17. Two samples were demonstrated for each mesh size. For 4-layer micro mesh wicking structures, there were mainly two distinct regions in the boiling curves, with evaporation dominated between low to moderate heat flux, and boiling dominated at high heat flux. The onset of nucleate boiling of 4-layer # 100 micro mesh was around 42.4 W/cm^2 for both samples, and the variation of temperature superheat during boiling regime

was less than 2 °C. However, the heat transfer coefficient of both samples was different, resulting from the variance in the effective pore sizes of different samples induced by stackings of micro mesh. The differences of the pore sizes and the wire diameters of # 145 mesh and # 200 mesh were within 20% and 10%, respectively, and therefore, # 145 and # 200 micro mesh exhibited similar heat transfer performance. Compared with the 4-layer # 100 micro mesh samples, the heat transfer coefficients of 4-layer # 145 and # 200 micro mesh samples were substantially higher due to increased exposed surface area for thin film evaporation during low to moderate heat fluxes, and during high heat fluxes, when the nucleate boiling dominated over evaporation, the increased solid-liquid areas also extended the three-phase contact lines when vapor bubbles formed inside micro mesh, and therefore further enhanced the heat transfer performance. The onset of nucleate boiling of # 145 and # 200 micro mesh wicking structure occurred at 28.5 W/cm^2, much lower than that of # 100 micro mesh at 42.4 W/cm^2. First of all, the obtained 4-layer # 145 and # 200 micro mesh samples were thicker than the 4-layer # 100 micro mesh samples, heat was more prune to accumulate between the substrate and mesh wires, so the superheat required for nucleation boiling could be achieved under a lower heat flux; secondly, there were more nucleation sites induced by the micro cavities formed at the contacting area between the copper substrate and micro wires.

While the heat transfer coefficient and onset of nucleate boiling were strongly affected by the mesh sizes; a finer mesh yielded to a higher heat transfer coefficient and earlier nucleate boiling (boiling incipience at lower heat flux), the measured

permeability and capillary pressure showed weak dependence on the mesh sizes, furthermore, the dryout heat flux remained the same for three different mesh sizes: # 100, # 145, and # 200 micro mesh, and the heat transfer coefficient of different samples with the same mesh sizes varied from each other.

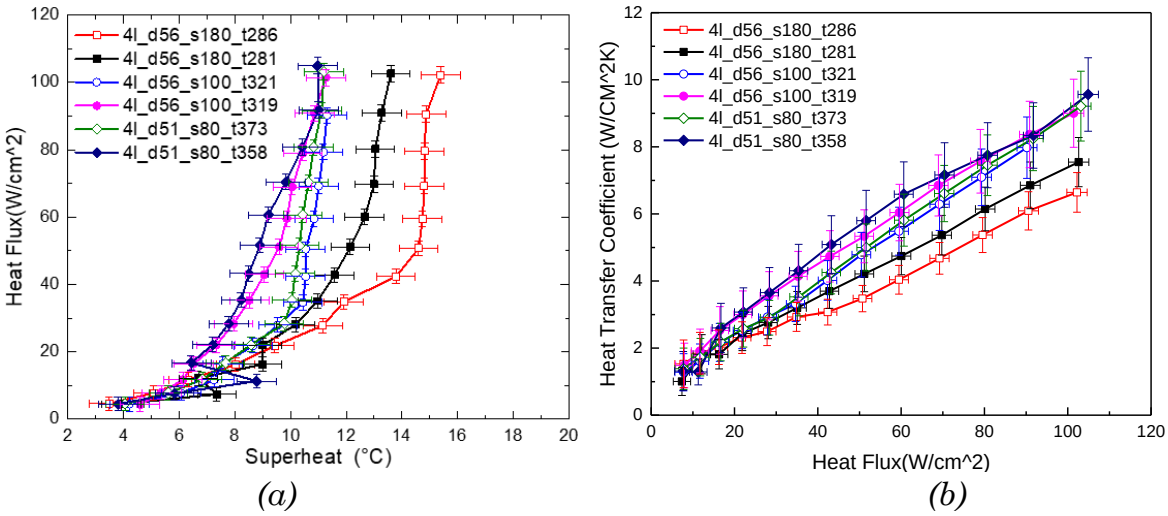

Fig. 3. 17 *The heat transfer performance of 4-layer micro mesh wicking structures with different mesh sizes (a) heat flux as a function of superheat (b) heat transfer coefficient as a function of heat flux*

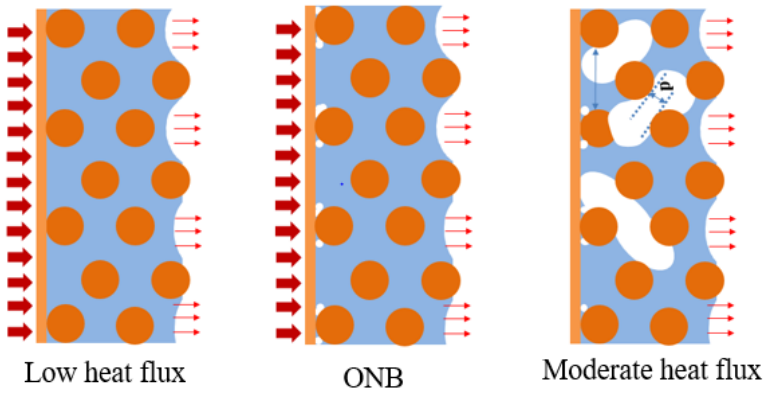

Fig. 3. 18 *Sketch of the wicking structure and liquid meniscus level for 6-layer mesh*

As shown in Fig. 3.18, when the applied heat flux was low, the heat transfer performance was determined by the evaporation, which could be affected by the exposed surface area that varied among different mesh sizes. However, as the applied heat flux increased, nucleate boiling became the dominant heat transfer mode, and the existence of vapor bubbles played an vital role in both heat transfer and liquid transport process. Fast vapor bubbles removal was required for enhancing multilayer micro mesh wicking structures. As shown in Fig. 3.18, the effective pores venting vapor bubbles were much smaller than the intrinsic openings between micro wires. And as shown in Fig. 3.16, coarse mesh with large inherent openings could have similar sized vapor venting path compared to a finer micro mesh due to the tendency to overlap more.

3.5.3 Enhanced Capillary Evaporation by Using Inline-Alignment

In the above discussions, the efficient vapor removal plays a dominant role in determining the heat transfer coefficient and the dryout heat flux of multilayer micro mesh wicking structures. While increasing the thickness of wicking structures could increase the cross-sectional area for flow passage and therefore reduce the flow resistance, leading to a higher capillary limit, however, the heat transfer performance was limited by the boiling limit caused by entrapped vapor bubbles. Additionally, while single-layer micro mesh of different mesh sizes owns different pore sizes, the pores for vapor venting of multilayer micro mesh could be similar due to alignment,

which has been neglected by most researchers but played a critical role in determining the heat transfer coefficient as well as the dryout heat flux of the multilayer micro mesh, in this thesis work, inline-aligned micro mesh with the maximum pores for vapor removal has been developed.

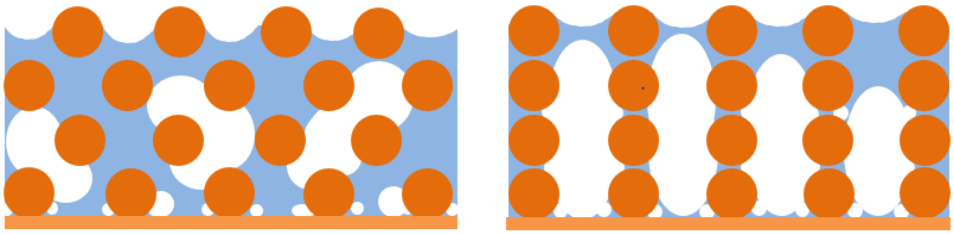

(a) (b)

Fig. 3. 19 *Schematic of cross-sectional view of staggered-aligned micro mesh and inline-aligned micro mesh (a) staggered-aligned micro mesh structure (b) inline-aligned micro mesh structure*

The schematic of the cross-sectional area of staggered-aligned and inline-aligned micro mesh wicking structures is shown in Fig. 3.19. Ideally, in staggered-aligned micro mesh, micro wires of every two neighboring layers offset by half of the openings between the micro wires, while in inline-aligned micro mesh, the micro wires of all layers aligned in a line. As shown in Fig. 3.19, taken # 100 mesh as an example, for the inline stacking, the pore size was similar to the intrinsic pore size of 180 μm, however, for staggered stacking, the pore size became much smaller, about half of the gap between the mesh wire and spacing, which was around 62 μm (0.5 × (180-56)), close to only 1/3 of the inline stacking. For # 145 mesh, the pore size of inline stacking based on idealized sketch was 100 μm, and it was around 22 μm for

staggered stacking, about 1/5 of the inline stacking. Besides of the large openings for fast vapor bubbles removal, the micro cavities between micro wires perpendicular to the substrate provide numerous active sites for nucleate boiling. So the inline-aligned micro mesh wicking structures could potentially increase both the heat transfer coefficient and the dryout heat flux. The SEM images of 4-layer staggered-aligned and inline-aligned micro mesh wicking structures are shown in Fig. 3.20.

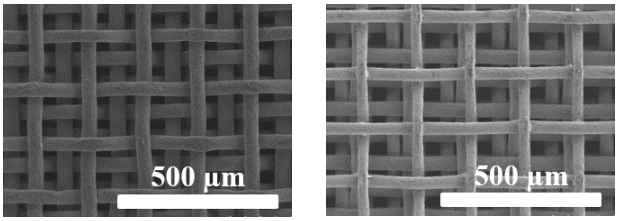

(a) (b)

Fig. 3.20 *SEM images of micro mesh with different alignments (a)4-layer # 100 inline-aligned micro mesh wicking structure (b) 4-layer # 100 staggered-aligned micro mesh wicking structure*

Table 3.3 *List of the micro mesh samples tested and their geometric properties*

Sample	Wire diameter	Spacing	Thickness	Porosity
4l_d56_s180_t286_Staggered	56 µm	180 µm	286 µm	0.522
4l_d56_s180_t280_Inline	56 µm	180 µm	280 µm	0.513
4l_d56_s100_t321_Staggered	56 µm	100 µm	321 µm	0.514
4l_d56_s100_t319_Inline	56 µm	100 µm	319 µm	0.527

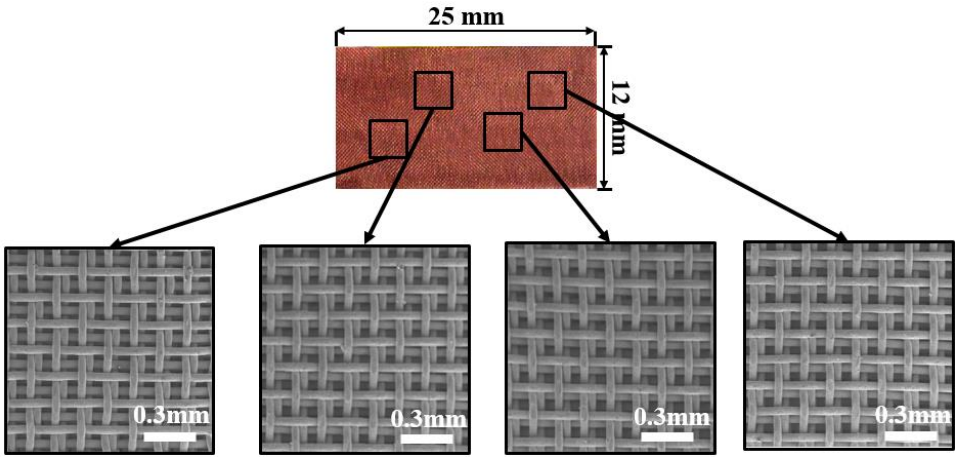

Fig. 3. 21 *The SEM images of a 4-layer inline-aligned # 145 micro mesh structure*

Details of the tested samples are shown in Table 3.4. And Fig. 3.21 shows an example of a 4-layer inline-aligned micro mesh wicking structure. It was slightly different from the idealized sketch due to the difficulty in fabrication, it was very challenging to align every single opening of the micro mesh, so the inline-aligned micro mesh referred to micro mesh with greater than 90% of the surface was inline-aligned. In addition, the inline-aligned micro wires were slightly offset than perfectly stacked right on the wires. But the openings for vapor venting were significantly larger than micro mesh with other alignments.

The permeability and the capillary pressure of the tested micro mesh samples are shown in Fig. 3.22, both were affected by the stackings. The staggered-aligned structure demonstrated higher capillary pressure than an inline-aligned structure. However, the permeability was much lower. The difference in permeability and capillary pressure caused by alignment became more apparent in micro mesh with a finer pore size, i.e., the difference in a 4-layer # 145 micro mesh was more significant than in a 4-layer # 100 micro mesh.

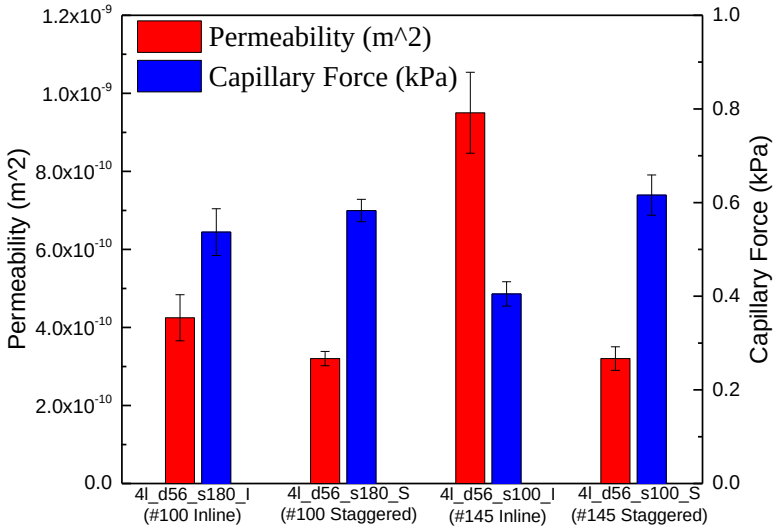

Fig. 3.22 *Permeability and capillary pressure of samples with different alignments*

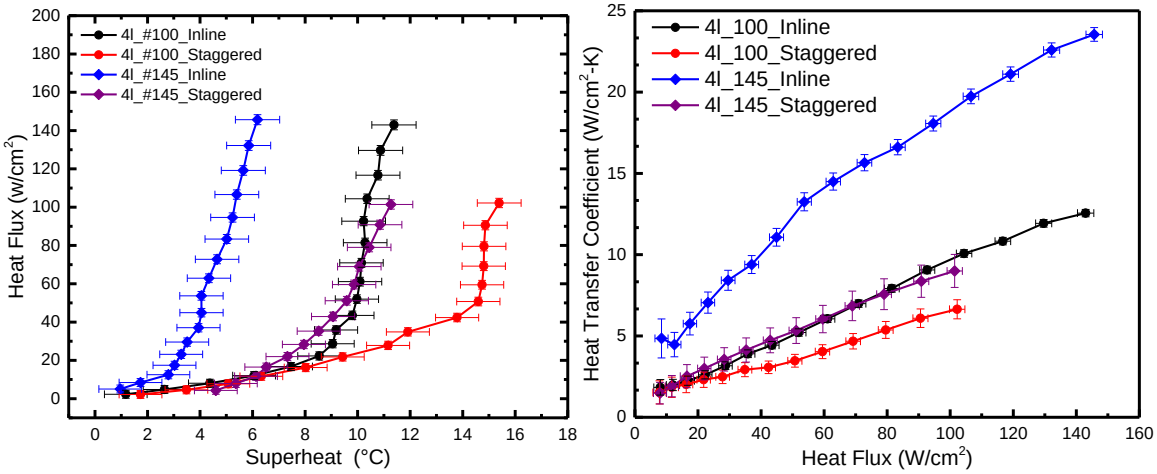

(a) *(b)*

Fig. 3.23 *The heat transfer performance of 4-layer micro mesh wicking structures with staggered and inline alignments (a) heat flux as a function of superheat (b) heat transfer coefficient as a function of applied heat flux*

The heat transfer performance of the tested samples is plotted in Fig. 3.23. For both mesh sizes, when the alignment of micro mesh changed from staggered to inline, the heat transfer performance was greatly enhanced. The dryout heat flux was increased by almost 50%, from around 100 W/cm^2 to about 150 W/cm^2; and the heat

transfer coefficient was doubled. The inline-aligned micro mesh had both increased nucleate boiling sites and enhanced vapor bubbles removal.

The micro cavities between micro wires in the direction perpendicular to the copper substrate could provide active nucleate sites under a lower superheat, and therefore, the onset of nucleate boiling of inline-aligned micro mesh was at lower heat flux 27.8 W/cm^2 compared with 42.8 W/cm^2 for staggered-aligned micro mesh, and the increased nucleation sites also improved the heat transfer coefficients. For 4-layer # 100 micro mesh, the maximum heat transfer coefficient was increased from 6.6 W/cm^2·K to 12.6 W/cm^2·K, and for 4-layer # 145 micro mesh, the maxim heat transfer coefficient was increased from 9.0 W/cm^2·K to 23.5 W/cm^2·K.

The heat transfer measurements were supplemented by the flow visualization study. The visualization of boiling in wicking structures was performed outside the teste chamber. Images were taken at 250 frames per second. At low heat flux, the heat transfer mode in both samples was thin film evaporation. As the heat flux increased, the inline-aligned micro mesh first started to nucleate at 27.8 W/cm^2, due to the large pores between the micro wires, vapor bubbles can easily escape from the micro mesh. However, the onset of nucleate boiling in staggered-aligned mesh occurred at 42.8 W/cm^2, and most vapor bubbles were constrained inside the micro mesh, with visible bubbles coming out of only less than 10% of the surface.

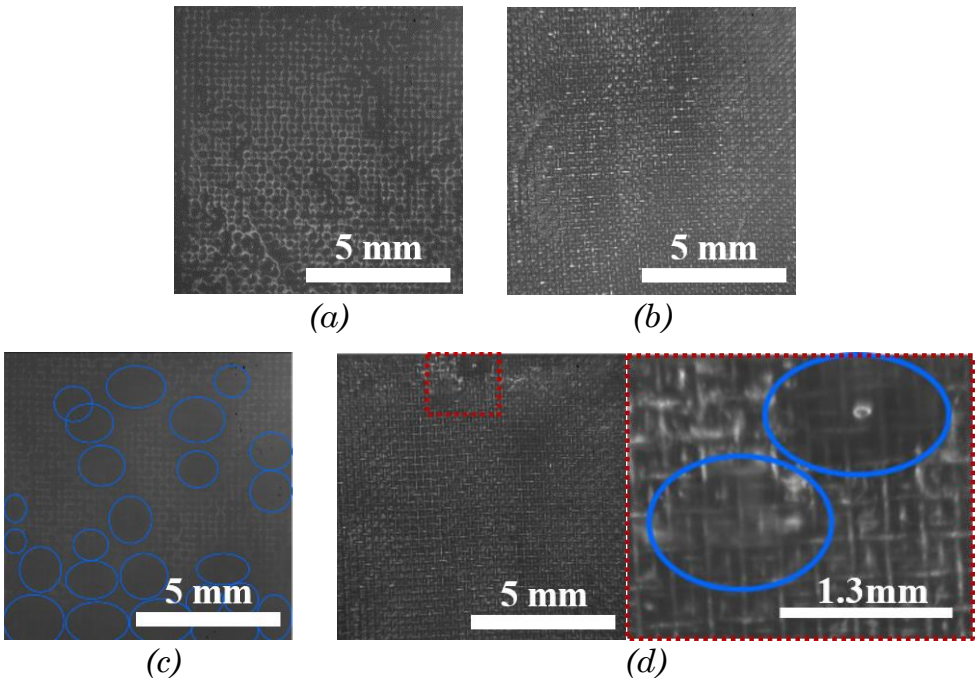

Fig. 3. 24 *Images of evaporation and nucleate boiling in 4-layer # 100 mesh*
(a) Example of the evaporation dominated regime of 4-layer # 100 inline-aligned micro mesh under a heat flux of $q = 7.8\ W/cm^2$ (b) Example of the evaporation dominated regime of 4-layer # 100 staggered-aligned micro mesh under a heat flux of $q = 7.8\ W/cm^2$ (c) transition from the evaporation dominated regime to the nucleate-boiling dominated regime of 4-layer # 100 inline-aligned micro mesh at a heat flux of $q = 27.8\ W/cm^2$ (d) transition from the evaporation dominated regime to the nucleate-boiling dominated regime of 4-layer # 100 inline-aligned micro mesh at a heat flux of $q = 42.8\ W/cm^2$

3.5.4 Enhanced Capillary Evaporation by Nanostructured Surfaces

Nanostructures [59][75][14][76][58] have been implemented on the surface of homogeneous wicking structures to enhance the capillary evaporation heat transfer performance, which is attributed to increased capillary pressure by decreasing the

contact angle subtended by the liquid while permeability remained identical to the base homogeneous wicking structure [46].

Current work developed two different nanostructures for enhancing the heat transfer performance of # 200 micro mesh wicking structures (wire diameter of 51 μm, spacing of 80 μm, and thickness of 103 μm), as shown in Fig. 3.25 (a) ~ (f). Type A nanostructures were formed by immersing the micro mesh samples in an alkali solution composed of $NaClO_2$(3.75g), NaOH(5g), $Na_3PO_4 \cdot 12H_2O$(10g), and deionized water(100ml), the solution was heated to 85°C, a thin (<200nm) Cu_2O layer first covered the entire surface of micro mesh, and then, grass-like CuO nanostructures were grown on this layer, the growing process was self-limiting, with the obtained nanostructures thinner than 3 μm. Type B nanostructures were obtained by two steps, the first step was the same as the process for type A nanostructures, and then the micro mesh sample was cleaned in 2wt% dilute sulfuric acid to remove the grass-like nanostructures, followed by dipping the sample in dilute acid piranha for etching, the obtained nanotexture was pebble-like, as shown in Fig. 3.25 (f).

As shown in Fig 3.26, the implementation of nanostructures increased the wicking speed of micro mesh, and type B nanostructure exhibited faster wicking compared with the other two surfaces. The results in Fig. 3.27 indicate that nanostructures didn't alter the permeability of the micro mesh wicking structure, and nanostructured surface slightly improved the capillary force.

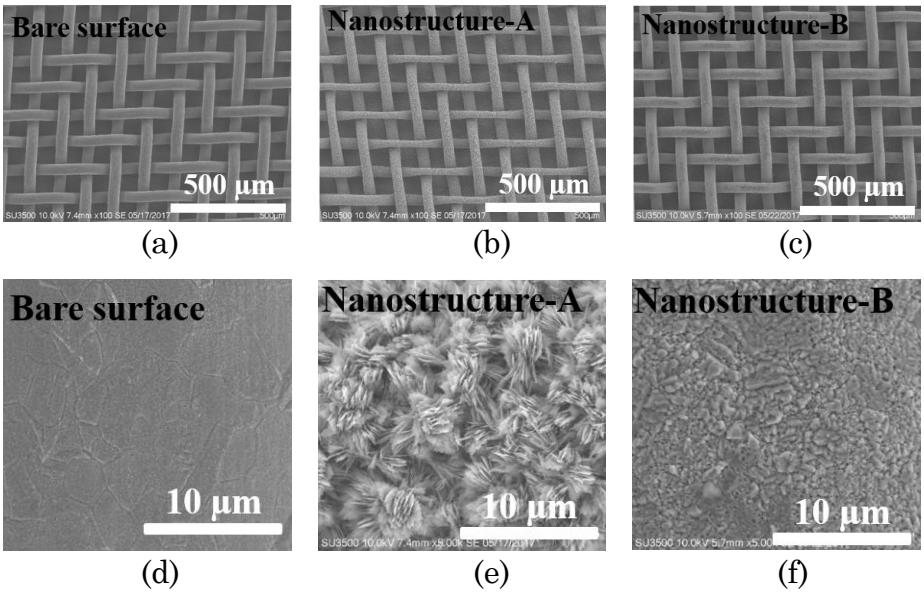

Fig. 3.25 *The SEM images of micro mesh samples with different surface structures (a) micro mesh with bare surface (b) micro mesh with type A nanostructure (c) micro mesh with type B nanostructure (d) surface profile of bare surface (e) surface profile of type A nanostructure (f) surface profile of type B nanostructure*

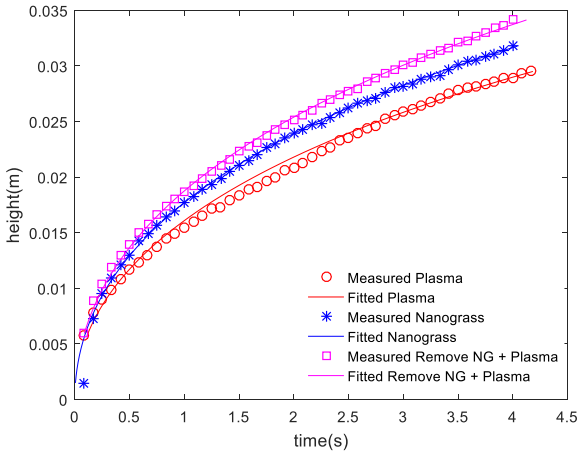

Fig. 3.26 *Capillary rate of rise performance of single-layer # 200 micro mesh with different surface structures (bare surface, nanostructure A and nanostructure B)*

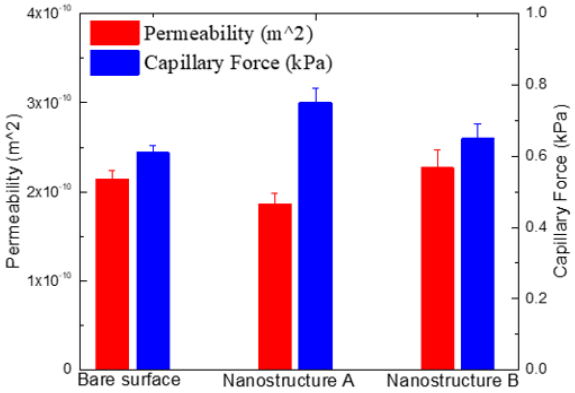

Fig. 3.27 *The permeability and capillary force of single-layer # micro mesh with different surface structures (bare surface, nanostructure A and nanostructure B)*

The thermal performance of single-layer # 200 micro mesh wicking structure is presented in Fig. 3.28. The sample with bare surface operated until 13.4 W/cm^2, and sample with grass-like nanostructure (A) operated until heat load of 11.0 W/cm^2, similar to the value reported in [47]. However, the sample with pebble-like nanostructure (B) demonstrated a much higher dryout out heat flux, and it could operate until 48.5 W/cm^2. When the heat flux was lower than 15 W/cm^2, the heat transfer coefficient of these three samples were identical, as the heat flux increased, while samples with bare surface and grass-like nanostructure dried out, the sample with pebble-like nanostructure could continue to supply liquid to the evaporator, and as the liquid meniscus receded, the capillary pressure increased, and the heat transfer performance was enhanced due to stronger evaporation. When the heat flux exceeded 44.2 W/cm^2, the sample experienced partial dryout.

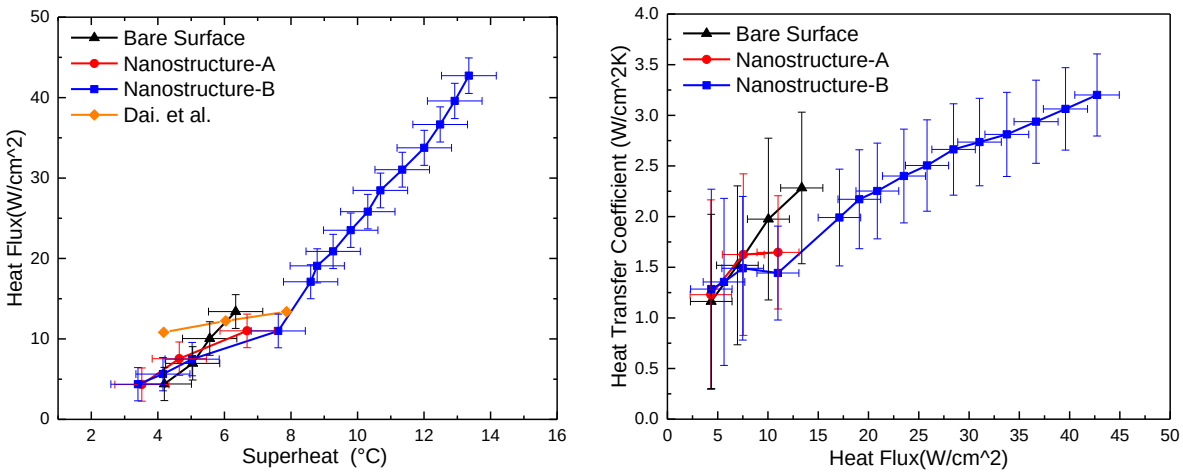

Fig. 3.28 *The heat transfer curves of single-layer # 200 micro mesh structure (a) heat flux as a function of superheat (b) heat transfer coefficient as a function of heat flux*

Although implementation of nanostructures could reduce the contact angle between water and copper/copper oxide, oxygen plasma treatment of bare surface could yield a comparably small contact angle, so the intrinsic permeability and capillary pressure were primarily determined by the macroscopic features of micro mesh including wire diameter and spacing, and therefore, the obtained permeability and capillary pressure of those three samples were similar. However, as the heat flux increased, the evaporation intensified, and the liquid meniscus receded close to the copper substrate, the micro-/nano-scale features in the openings between micro wires enabled by pebble-like nanostructures demonstrated advantageous performance compared with grass-like nanostructured surface and bare surface by enhancing the capillary wicking performance and improving the evaporation heat transfer by enlarging the surface area.

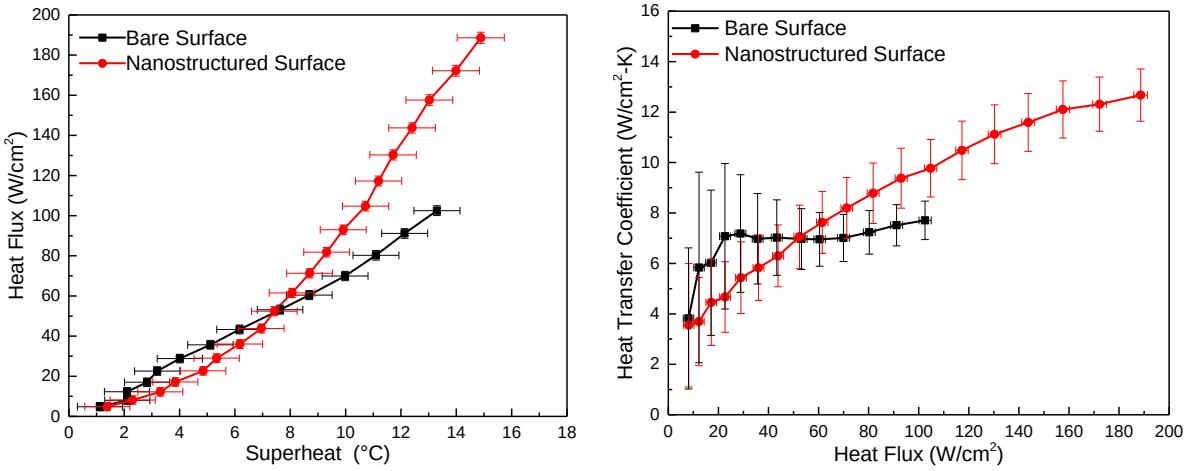

Fig. 3. 29 *The heat transfer performance of 4-layer # 200 micro mesh wicking structures (a) heat flux as a function of superheat (b) heat transfer coefficient as a function of applied heat flux*

As pebble-like nanostructured surface significantly promoted the heat transfer performance of single-layer # 200 micro mesh wicking structure, it has been implemented onto 4-layer # 200 micro mesh wicking structure. And the test results were presented in Fig. 3.29. As the heat flux was smaller than 50W/cm^2, 4-layer micro mesh wicking structure with nanostructured surface had lower heat transfer coefficient due to the larger thermal resistance of liquid film induced by enhanced wicking. However, as the heat flux became larger, the micro- and nano-scale cavities provided by the nanostructured surface could provide active nucleate sites under different superheat, leading to higher heat transfer coefficient. And the better liquid supply of nanostructured surface also contributed to a higher dryout heat flux of 188.6 W/cm^2 for 4-layer micro mesh, compared with a dryout heat flux of 102.5 W/cm^2 for the sample without nanostructures.

CHAPTER 4 SUMMARY AND FUTURE WORK

The objective of the current work was to further understand the fundamental fluid and heat transport mechanisms in scalable and low-cost micro mesh wicking structures and to thereby improve the design and performance capabilities of ultra-thin TGPs. Ultra-thin TGPs with thickness around 0.30-mm have been developed. With all the applied power, the effective thermal conductivity of five ultra-thin TGP prototypes was higher than a copper reference. For a heater of size 8 mm × 8mm, the maximum effective thermal conductivity of the best-performed ultra-thin TGP was around 2600 W/m-K at an applied power of 10.5 W, greater than six times that of a copper reference. The maximum effective thermal conductivity of all ultra-thin TGP prototypes exceeded 1200 W/m-K, about three times that of a copper reference.

The effects of geometric parameters including the layers thickness and mesh sizes on the capillary wicking and the heat transfer performance of micro mesh wicking structures have been studied, and based on these understandings, two different methods have been developed to improve the performance of multilayer micro mesh wicking structure by using inline-aligned micro mesh and nanostructured surface, respectively. With inline-aligned micro mesh, the dryout heat flux was increased by 50%, and the heat transfer coefficient of 4-layer # 145

micro mesh was increased by three times. With the implementation of nanostructured surface, the dryout heat flux of single-layer micro mesh wicking structure as increased by more than three times, while that of 4-layer micro mesh was increased by about 90%.

4.1 Summary for TGPs

Ultra-thin TGPs with a thickness of around 0.30-mm have been developed. The active area was 10 cm × 5 cm. Over a heating area of 8 mm × 8 mm, five TGP prototypes demonstrated dryout power ranging from 6.5 W to 7.5 W with chiller set to 12 °C, with a warmer condenser, the thermal resistance of TGP prototypes was reduced significantly, and the dryout power was increased. During the experiments, the dryout condition wasn't reached with a warmer condenser as the evaporator temperature of TGP prototypes already exceeded 70 °C, further increase of which could potentially destroy the TGP devices.

A hybrid wicking structure has been developed by bonding single-layer # 500 stainless steel micro mesh bonded onto copper micro pillars via electroplating, which not only encapsulated stainless steel wires with copper to prevent corrosion but also created microtextured surfaces formed by copper flakes which increased capillary force and promoted capillary evaporation by adding surface areas.

With all the power tested under both cooler and warmer condenser, the effective thermal conductivity of TGP prototypes was higher than a copper reference. And the maximum effective thermal conductivity of the best-performed ultra-thin

TGP was around 2600 W/m-K at an applied power of 10.5 W, higher than six times that of a copper reference. TGP prototypes also showed excellent reliability with no degradation after 45 days.

4.2 Summary for Capillary Evaporation

Experimental methodologies to determine the permeability and capillary pressure of multilayer micro mesh wicking structures have been developed

- The permeability and capillary pressure of multilayer micro mesh wicking structure showed weak dependence on the tested samples with different mesh sizes, so the analytical expressions based on perfectly inline aligned micro mesh resulted in significant under/over-prediction of these properties; experimental measurements should be used to accurately characterize such wicking structures;
- The rate of rise experiments have been conducted to obtain the liquid front height as a function of time, and by non-linear regression in Matlab, both permeability and capillary pressure values could be extracted. The uncertainty of most measurements was below 10%.
- An experimental facility was developed that fed liquid to the wicking structure by capillary action. This facility was used to determine the dryout heat flux and heat transfer coefficient across an evaporating/boiling micro mesh wicking structure with varying properties.
- The dryout heat flux of double-layer micro mesh wicking structure was 67.5 W/cm^2; boiling wasn't observed during the measurement. However, as the

number of layers increased to four, nucleate boiling occurred at 42.4 W/cm^2, which greatly enhanced the heat transfer performance. Further increase in the thickness brought boiling incipience at lower heat flux. However, it didn't increase the dryout heat flux further due to constrained vapor bubbles experiencing greater resistance to escape.

- The mesh sizes (# 100, # 145, and # 200) investigated in current work didn't affect the dryout heat flux due to similar pore sizes for vapor bubbles venting caused by the alignment. However, finer mesh showed higher heat transfer coefficients. And the onset of nucleate boiling in both 4-layer # 145, and 4-layer # 200 micro mesh occurred at lower heat flux compared with a 4-layer # 100 micro mesh.
- Through the inline-alignment, the dryout heat flux of both 4-layer # 100 micro mesh and 4-layer # 145 micro mesh was increased by 50%, and the heat transfer coefficient of 4-layer # 100 micro mesh and 4-layer # 145 micro mesh was increased to twice and three times, respectively.
- By implementing pebble-like nanostructures on micro mesh wicking structures, for a heater of size 10 mm × 10 mm with water level 15 mm below the heater centerline, the dryout heat flux of single-layer # 200 micro mesh wicking structure was increased from 13.4 W/cm^2 to 44.2 W/cm^2, and the dryout heat flux of 4-layer # 200 micro mesh wicking structure was increased from 102.5 W/cm^2 to 188.6 W/cm^2.

4.3 Future Work

Plans for future work are outlined. Several possible experimental studies are proposed to further improve the multilayer micro mesh wicking structure.

- While the capillary rate of rise experiments in the current study are appropriate for thick micro mesh wicking structures, the analysis is not valid for smaller pores and thin wicking structures, which has a low permeability causing the liquid front to rise slowly. Furthermore, for thin wicking structures that have a large surface area to volume ratio, evaporation from the sample to ambient governs the liquid front speed and can no longer be neglected.
- In the current study, the alignment of micro mesh has been demonstrated to influence significantly both the heat transfer coefficient and dryout heat flux of multilayer micro mesh wicking structures, however, due to the challenges in the fabrication of inline-aligned micro mesh, only two samples with such alignment have been fabricated for measurements. To better understand the effect of alignment, the way to precisely control the alignment of micro mesh needs to be developed.
- In order to achieve high heat flux, thick micro mesh wicking structures are required, of which the onset of nucleate boiling significantly enhance the heat transfer performance. Other geometric designs can be used to promote nucleation sites and vapor removal.

REFERENCES

[1] J. Millan, P. Godignon, X. Perpina, A. Perez-Tomas, and J. Rebollo, "A Survey of Wide Bandgap Power Semiconductor Devices," IEEE Trans. Power Electron., vol. 29, no. 5, pp. 2155–2163, 2014.

[2] S. Adera, D. Antao, R. Raj, and E. N. Wang, "Thin-Film Evaporation from Micropillar Wicks in Ambient Environment," 2017.

[3] Q. Li, A. Han, G. Yang, Y. Hong, Z. Zhang, L. Jin, and J. Yang, "Technical Challenges and Novel Passive Cooling Technologies for Ultra-Thin Notebooks," 2017.

[4] Faghri Amir, Heat Pipe Science and Technology. Taylor & Francis, 1995.

[5] D. A. Reay and P. A. Kew, Heat Pipes: Theory, Design and Applications, Fifth Edit. Butterworth Heinemann, 2007.

[6] G. Patankar, S. Mancin, J. A. Weibel, S. V. Garimella, and M. A. MacDonald, "A Method for Thermal Performance Characterization of Ultrathin Vapor Chambers Cooled by Natural Convection," J. Electron. Packag., vol. 138, no. 1, p. 10903, 2016.

[7] G. Patankar, J. A. Weibel, and S. V. Garimella, "Patterning the condenser-side wick in ultra-thin vapor chamber heat spreaders to improve skin temperature uniformity of mobile devices," Int. J. Heat Mass Transf., vol. 101, pp. 927–936, 2016.

[8] R. Ranjan, R. Ranjan, J. Y. Murthy, S. V Garimella, D. H. Altman, and M. T. North, "Modeling and Design Optimization of Ultra-Thin Vapor Chambers for High Heat Flux Applications Modeling and Design Optimization of Ultrathin Vapor Chambers for High Heat Flux Applications," 2012.

[9] Y. Yadavalli, Y. Yadavalli, J. A. Weibel, and S. V Garimella, "Performance-Governing Transport Mechanisms for Heat Pipes at Ultra-thin Form Factors Performance-Governing Transport Mechanisms for Heat Pipes at Ultra-Thin Form Factors," 2015.

[10] G. Patankar, J. A. Weibel, and S. V Garimella, "Working-fluid selection for minimized thermal resistance in ultra-thin vapor chambers," Int. J. Heat Mass Transf., 2016.

[11] C. Ding, G. Soni, P. Bozorgi, B. D. Piorek, C. D. Meinhart, and N. C. MacDonald, "A flat heat pipe architecture based on nanostructured titania," J. Microelectromechanical Syst., vol. 19, no. 4, pp. 878–884, 2010.

[12] R. Lewis, S. Xu, L. A. Liew, C. Coolidge, R. Yang, and Y. C. Lee, "Thin Flexible Thermal Ground Planes: Fabrication and Scaling Characterization," J. Microelectromechanical Syst., vol. 24, no. 6, pp. 2040–2048, 2015.

[13] R. Lewis, L.-A. Liew, S. Xu, Y. C. Lee, and R. Yang, "Microfabricated ultra-thin all-polymer thermal ground planes," Sci. Bull., vol. 60, no. 7, pp. 701–706, 2015.

[14] C. Ding, P. Bogorzi, N. Srivastava, M. Sigurdson, C. Meinhart, and N. C. MacDonald, "Super wetting of micro&nano structured titania surfaces,"

TRANSDUCERS 2009 - 15th Int. Conf. Solid-State Sensors, Actuators Microsystems, pp. 401–404, 2009.
[15] C. Oshman, B. Shi, C. Li, R. Yang, Y. C. Lee, G. P. Peterson, and V. M. Bright, "The development of polymer-based flat heat pipes," J. Microelectromechanical Syst., vol. 20, no. 2, pp. 410–417, 2011.
[16] C. Oshman, Q. Li, L.-A. Liew, R. Yang, V. M. Bright, and Y. C. Lee, "Flat flexible polymer heat pipes," J. Micromechanics Microengineering, vol. 23, no. 1, p. 15001, 2013.
[17] C. Oshman, Q. Li, L.-A. Liew, R. Yang, Y. C. Lee, V. M. Bright, D. J. Sharar, N. R. Jankowski, and B. C. Morgan, "Thermal performance of a flat polymer heat pipe heat spreader under high acceleration," J. Micromechanics Microengineering, vol. 22, no. 4, p. 45018, 2012.
[18] R. Lewis, L.-A. Liew, S. Xu, Y.-C. Lee, and R. Yang, "Microfabricated ultra-thin all-polymer thermal ground planes," Sci. Bull., vol. 60, no. 7, pp. 701–706, Apr. 2015.
[19] L.-A. Liew, C.-Y. Lin, R. Lewis, S. Song, Q. Li, R. Yang, and Y. C. Lee, "Flexible Thermal Ground Planes Fabricated With Printed Circuit Board Technology," J. Electron. Packag., vol. 139, no. 1, p. 11003, 2016.
[20] Y. Li, J. He, H. He, Y. Yan, Z. Zeng, and B. Li, "Investigation of ultra-thin flattened heat pipes with sintered wick structure," Appl. Therm. Eng., vol. 86, pp. 106–118, 2015.
[21] J. Li and L. Lv, "Experimental studies on a novel thin flat heat pipe heat spreader," Appl. Therm. Eng., vol. 93, pp. 139–146, 2016.
[22] Q. Cai, B. Chen, and C. Tsai, "Design, development and tests of high-performance silicon vapor chamber," J. Micromechanics Microengineering, vol. 22, no. 3, p. 35009, 2012.
[23] Q. Cai, B.-C. Chen, C. Tsai, and C. Chen, "Development of Scalable Silicon Heat Spreader for High Power Electronic Devices," J. Therm. Sci. Eng. Appl., vol. 1, no. 4, p. 41009, 2009.
[24] S. Q. Cai, Y. C. Chen, and A. Bhunia, "Design, development and tests of a compact thermofluid system," Appl. Therm. Eng., vol. 102, pp. 1320–1327, 2016.
[25] Y. Tang, D. Yuan, L. Lu, and Z. Wang, "A multi-artery vapor chamber and its performance," Appl. Therm. Eng., vol. 60, no. 1–2, pp. 15–23, 2013.
[26] B. Holley and A. Faghri, "Permeability and effective pore radius measurements for heat pipe and fuel cell applications," 2005.
[27] C. Zhang and K. E. Goodson, "characterization of the capillary performance of copper inverse opals," pp. 1–8, 2017.
[28] C. Byon and S. J. Kim, "Capillary performance of bi-porous sintered metal wicks," Int. J. Heat Mass Transf., vol. 55, pp. 4096–4103, 2012.
[29] D. R. Adkins, T. A. Moss, C. E. Andraka, N. H. Andreas, and H. M. Cole, "An examination of metal felt wicks for heat-pipe applications," in Proceedings of the 1995 ASME/JSME/JSES International Solar Energy Conference, 1995, pp. 553–558.

[30] R. R. Williams and D. K. Harris, “Cross-plane and in plane porous properties measurements of thin metal felts: applications in heat pipes,” Exp. Therm. Fluid Sci., vol. 27, no. 3, pp. 227–235, 2003.
[31] Kozai Hiroaki, Imura Hideaki, and Ikeda Yuji, “The Permeability of Screen Wicks,” JSME Int. J., vol. 34, 1991.
[32] H. Noda, Yoshioka Keisuke, and T. Hamatake, “An Experimental Study on the Permeability of Screen Wicks,” JSME Int. J., vol. 36, 1993.
[33] C. Zhang, G. Rong, J. W. Palko, T. J. Dusseault, M. Asheghi, J. G. Santiago, and Goo, “Tailoring of permeability in copper inverse opal for electronic cooling applications,” in Proceedings of the ASME 2015 International Technical Conference and Exhibition on Packaging and Integration of Electronic and Photonic Microsystems, 2015.
[34] N. Fries, K. Odic, M. Conrath, and M. Dreyer, “The effect of evaporation on the wicking of liquids into a metallic weave,” J. Colloid Interface Sci., vol. 321, no. 1, pp. 118–129, 2008.
[35] A. Rogacs, J. E. Steinbrenner, J. A. Rowlette, J. M. Weisse, X. L. Zheng, and K. E. Goodson, “Characterization of the wettability of thin nanostructured films in the presence of evaporation,” J. Colloid Interface Sci., vol. 349, no. 1, pp. 354–360, 2010.
[36] S. Adera, D. Antao, R. Raj, and E. N. Wang, “Design of micropillar wicks for thin-film evaporation,” Int. J. Heat Mass Transf., vol. 101, pp. 280–294, 2016.
[37] Y. Zhu, D. S. Antao, Z. Lu, S. Somasundaram, T. Zhang, and E. N. Wang, “Prediction and Characterization of Dry-out Heat Flux in Micropillar Wick Structures,” Langmuir, vol. 32, no. 7, pp. 1920–1927, 2016.
[38] D. Horner, “HT2013-17593,” pp. 1–6, 2017.
[39] S. Ravi, D. Horner, and S. Moghaddam, “Mass transport characteristics and theoretical performance limits of micropillar wicks,” Thermomechanical Phenom. Electron. Syst. -Proceedings Intersoc. Conf., pp. 1228–1234, 2014.
[40] M. a. Hanlon and H. B. Ma, “Evaporation Heat Transfer in Sintered Porous Media,” J. Heat Transfer, vol. 125, no. 4, p. 644, 2003.
[41] T. W. Davis and S. V Garimella, “Experimental Heat Transfer Thermal Resistance Measurement across a Wick Structure Using a Novel Thermosyphon Test Chamber,” Exp. Heat Transf., vol. 21, pp. 143–154, 2008.
[42] T. Semenic, Y. Y. Lin, I. Catton, and D. B. Sarraf, “Use of biporous wicks to remove high heat fluxes,” 2007.
[43] J. A. Weibel, S. V. Garimella, and M. T. North, “Characterization of evaporation and boiling from sintered powder wicks fed by capillary action,” Int. J. Heat Mass Transf., vol. 53, no. 19–20, pp. 4204–4215, 2010.
[44] J. A. Weibel and S. V Garimella, “Visualization of vapor formation regimes during capillary-fed boiling in sintered-powder heat pipe wicks,” Int. J. Heat Mass Transf., vol. 55, pp. 3498–3510, 2012.
[45] S. Adera, R. Raj, and E. N. Wang, “MNHMT2013-22120,” pp. 1–7, 2017.
[46] S. Ravi, R. Dharmarajan, and S. Moghaddam, “Physics of Fluid Transport in Hybrid Biporous Capillary Wicking Microstructures.”

[47] X. Dai, F. Yang, R. Yang, Y. C. Lee, and C. Li, "Micromembrane-enhanced capillary evaporation," Int. J. Heat Mass Transf., vol. 64, pp. 1101–1108, 2013.
[48] X. Dai, M. Famouri, A. I. Abdulagatov, R. Yang, Y.-C. Lee, S. M. George, and C. Li, "Capillary evaporation on micromembrane-enhanced microchannel wicks with atomic layer deposited silica," Cit. Appl. Phys. Lett. Phys. Lett. Appl. Phys. Lett. Appl. Phys. Lett, vol. 1031, no. 10, 2013.
[49] X. Dai, F. Yang, R. Yang, X. Huang, W. A. Rigdon, X. Li, and C. Li, "Biphilic nanoporous surfaces enabled exceptional drag reduction and capillary evaporation enhancement," Cit. Appl. Phys. Lett. Phys. Lett. Phys. Lett. Appl. Phys. Lett, vol. 1051, no. 10, 1916.
[50] M. T. North, J. H. Rosenfeld, and R. . Shaubach, "Liquid film evaporation from bidisperse capillary wicks in heat pipe evaporators," in Proceedings of the 9th International Heat Pipe Conference, 1995.
[51] T. Semenic, Y. Y. Lin, I. Catton, and D. B. Sarraf, "Use of biporous wicks to remove high heat fluxes," Appl. Therm. Eng., vol. 28, no. 4, pp. 278–283, 2008.
[52] Y. Zhao and C. Chen, "An Investigation of Evaporation Heat Transfer in Sintered Copper Wicks With Microgrooves," pp. 1–5, 2017.
[53] G. S. Hwang, Y. Nam, E. Fleming, P. Dussinger, Y. S. Ju, and M. Kaviany, "Multi-artery heat pipe spreader: Experiment," Int. J. Heat Mass Transf., vol. 53, no. 13–14, pp. 2662–2669, 2010.
[54] G. S. Hwang, E. Fleming, B. Carne, S. Sharratt, Y. Nam, P. Dussinger, Y. S. Ju, and M. Kaviany, "Multi-artery heat-pipe spreader: Lateral liquid supply," 2011.
[55] Y. S. Ju, M. Kaviany, Y. Nam, S. Sharratt, G. S. Hwang, I. Catton, E. Fleming, and P. Dussinger, "Planar vapor chamber with hybrid evaporator wicks for the thermal management of high-heat-flux and high-power optoelectronic devices," Int. J. Heat Mass Transf., vol. 60, no. 1, pp. 163–169, 2013.
[56] D. Ćoso, V. Srinivasan, M.-C. Lu, J.-Y. Chang, and A. Majumdar, "Enhanced Heat Transfer in Biporous Wicks in the Thin Liquid Film Evaporation and Boiling Regimes," J. Heat Transfer, vol. 134, no. 10, p. 101501, 2012.
[57] Q. Cai and A. Bhunia, "High heat flux phase change on porous carbon nanotube structures," Int. J. Heat Mass Transf., vol. 55, no. 21–22, pp. 5544–5551, 2012.
[58] Y. Nam, S. Sharratt, G. Cha, and Y. S. Ju, "Characterization and Modeling of the Heat Transfer Performance of Nanostructured Cu Micropost Wicks," J. Heat Transfer, vol. 133, no. 10, p. 101502, 2011.
[59] J. A. Weibel, S. S. Kim, T. S. Fisher, and S. V Garimella, "Carbon Nanotube Coatings for Enhanced Capillary- Fed Boiling from Porous Microstructures," Nanoscale Microscale Thermophys. Eng., vol. 16, pp. 1–17, 2012.
[60] A. S. Kousalya, J. A. Weibel, S. V. Garimella, and T. S. Fisher, "Metal functionalization of carbon nanotubes for enhanced sintered powder wicks," Int. J. Heat Mass Transf., vol. 59, no. 1, pp. 372–383, 2013.

[61] A. Brautsch and P. A. Kew, “Examination and visualisation of heat transfer processes during evaporation in capillary porous structures,” Appl. Therm. Eng., vol. 22, no. 7, pp. 815–824, 2002.
[62] C. Li, G. P. Peterson, and Y. Wang, “Evaporation/Boiling in Thin Capillary Wicks (l)—Wick Thickness Effects,” J. Heat Transfer, vol. 128, no. 12, p. 1312, 2006.
[63] C. Li, G. P. Peterson, and Y. Wang, “Evaporation/Boiling in Thin Capillary Wicks (ll)——Effects of Volumetric Porosity and Mesh Size,” J. Heat Transfer, vol. 128, no. 12, p. 1312, 2006.
[64] Y. H. Diao, Y. Liu, Y. H. Zhao, and S. Wang, “Evaporation/Boiling Heat Transfer Performance in a Sintered Copper Mesh Structure,” J. Heat Transfer, vol. 136, no. August, p. 81502, 2014.
[65] R. S. Hale, R. T. Bonnecaze, and C. H. Hidrovo, “Optimization of capillary flow through square micropillar arrays,” Int. J. Multiph. Flow, vol. 58, pp. 39–51, 2014.
[66] K. Yazdchi, S. Srivastava, and S. Luding, “Microstructural effects on the permeability of periodic fibrous porous media,” Int. J. Multiph. Flow, vol. 37, pp. 956–966, 2011.
[67] K. Yazdchi, S. Srivastava, and S. Luding, “Micro-macro relations for flow through random arrays of cylinders,” Compos. Part A, vol. 43, pp. 2007–2020, 2012.
[68] A. Tamayol and M. Bahrami, “Analytical determination of viscous permeability of fibrous porous media,” Int. J. Heat Mass Transf., vol. 52, pp. 2407–2414, 2009.
[69] R. Ranjan, A. Patel, S. V Garimella, and J. Y. Murthy, “Wicking and thermal characteristics of micropillared structures for use in passive heat spreaders,” Int. J. Heat Mass Transf., vol. 55, pp. 586–596, 2012.
[70] R. Xiao and E. N. Wang, “Microscale Liquid Dynamics and the Effect on Macroscale Propagation in Pillar Arrays,” Langmuir, vol. 27, pp. 10360–10364, 2011.
[71] C. Byon and S. J. Kim, “The effect of meniscus on the permeability of micro-post arrays,” J. Micromechanics Microengineering, vol. 21, no. 11, p. 115011, 2011.
[72] L. H. Chien and C. C. Chang, “Experimental study of evaporation resistance on porous surfaces in flat heat pipes,” Intersoc. Conf. Therm. Thermomechanical Phenom. Electron. Syst. ITHERM, vol. 2002–Janua, pp. 236–242, 2002.
[73] Y. Zhao and C. Chen, “An Investigation of Evaporation Heat Transfer in Sintered Copper Wicks With Microgrooves,” Proc. IMECE2006 2006 ASME Int. Mech. Eng. Congr. Expo., pp. 177–181, 2006.
[74] J. W. Palko, C. Zhang, J. D. Wilbur, T. J. Dusseault, M. Asheghi, K. E. Goodson, and J. G. Santiago, “Approaching the limits of two-phase boiling heat transfer: High heat flux and low superheat,” Appl. Phys. Lett., vol. 107, no. 25, 2015.

[75] A. S. Zuruzi, H. C. Gardner, A. J. Monkowski, and N. C. Macdonald, “Tailored nanostructured titania integrated on titanium micropillars with outstanding wicking properties,” vol. 13, 2013.
[76] Y. Nam, S. Sharratt, C. Byon, S. J. Kim, and Y. S. Ju, “Fabrication and characterization of the capillary performance of superhydrophilic Cu micropost arrays,” J. Microelectromechanical Syst., vol. 19, no. 3, pp. 581–588, 2010.
[77] Q. Cai and Y.-C. Chen, “Investigations of Biporous Wick Structure Dryout,” J. Heat Transfer, vol. 134, no. 2, p. 21503, 2012.
[78] X. L. Cao, ¤ P Cheng, and T. S. Zhao, “Experimental Study of Evaporative Heat Transfer in Sintered Copper Bidispersed Wick Structures,” J. Thermophys. HEAT Transf., vol. 16, no. 4.
[79] C. Byon and S. J. Kim, “Study on the capillary performance of micro-post wicks with non-homogeneous configurations,” Int. J. Heat Mass Transf., vol. 68, pp. 415–421, 2014.
[80] T. Semenic and I. Catton, “Experimental study of biporous wicks for high heat flux applications,” Int. J. Heat Mass Transf., vol. 52, no. 21–22, pp. 5113–5121, 2009.
[81] Y. X. Wang and G. P. Peterson, “Analytical Model for Capillary Evaporation Limitation in Thin Porous Layers,” J. Thermophys. HEAT Transf., vol. 17, no. 2.
[82] R. Kempers, D. Ewing, and C. Y. Ching, “Effect of number of mesh layers and fluid loading on the performance of screen mesh wicked heat pipes,” Appl. Therm. Eng., vol. 26, no. 5–6, pp. 589–595, 2006.
[83] S. C. Wong and Y. H. Kao, “Visualization and performance measurement of operating mesh-wicked heat pipes,” Int. J. Heat Mass Transf., vol. 51, no. 17–18, pp. 4249–4259, 2008.
[84] J. H. Liou, C. W. Chang, C. Chao, and S. C. Wong, “Visualization and thermal resistance measurement for the sintered mesh-wick evaporator in operating flat-plate heat pipes,” Int. J. Heat Mass Transf., vol. 53, no. 7–8, pp. 1498–1506, 2010.
[85] S.-C. Wong, J.-H. Liou, and C.-W. Chang, “Evaporation resistance measurement with visualization for sintered copper-powder evaporator in operating flat-plate heat pipes,” 2010.
[86] K. S. Yang, T. Y. Yang, C. W. Tu, C. T. Yeh, and M. T. Lee, “A novel flat polymer heat pipe with thermal via for cooling electronic devices,” Energy Convers. Manag., vol. 100, pp. 37–44, 2015.
[87] B. Shi, Y.-B. Wang, and Y.-J. Shan, “An Experimental Investigation of Thermal Performance of a Polymer-Based Flat Heat Pipe,” Heat Transf. Res., vol. 45, no. 8, pp. 746–757, 2016.
[88] G.-W. Wu, S.-L. Chen, and W.-P. Shih, “Lamination and Characterization of a Polyethylene-Terephthalate Flexible Micro Heat Pipe,” Front. Heat Pipes, vol. 3, pp. 80–85, 2012.
[89] S. S. Hsieh and Y. R. Yang, “Design, fabrication and performance tests for a

polymer-based flexible flat heat pipe," Energy Convers. Manag., vol. 70, pp. 10–19, 2013.
[90] X. Ji, H. Li, J. Xu, and Y. Huang, "Integrated flat heat pipe with a porous network wick for high-heat-flux electronic devices," 2017.
[91] L. Lv and J. Li, "Managing high heat flux up to 500 W/cm 2 through an ultra-thin flat heat pipe with superhydrophilic wick," Appl. Therm. Eng., vol. 122, pp. 593–600, 2017.
[92] C. Yang, C. Chang, C. Song, W. Shang, J. Wu, P. Tao, and T. Deng, "Fabrication and performance evaluation of flexible heat pipes for potential thermal control of foldable electronics," Appl. Therm. Eng., vol. 95, pp. 445–453, 2016.
[93] C. L. Hose, L. M. Boteler, J. Weyant, and B. Richard, "IPACK2017-74132 INTEGRATED VAPOR CHAMBER HEAT SPREADER FOR POWER MODULE," pp. 1–6, 2017.
[94] S. Lips, V. Sartre, F. Evre, S. Khandekar, and J. Bonjour, "OVERVIEW OF HEAT PIPE STUDIES DURING THE PERIOD 2010–2015," Interfacial Phenom. Heat Transf., vol. 4, no. 1, pp. 33–53, 2016.
[95] J. Qu, H. Wu, P. Cheng, Q. Wang, and Q. Sun, "Recent advances in MEMS-based micro heat pipes," 2017.
[96] M. Sigurdson, Y. Liu, P. Bozorgi, D. Bothman, N. MacDonald, and C. Meinhart, "A large scale Titanium Thermal Ground Plane," Int. J. Heat Mass Transf., vol. 62, no. 1, pp. 178–183, 2013.
[97] A. Bar-Cohen, K. Matin, N. Jankowski, and D. Sharar, "Two-Phase Thermal Ground Planes: Technology Development and Parametric Results," J. Electron. Packag., vol. 137, no. 1, p. 10801, 2015.
[98] N. Fries and M. Dreyer, "An analytic solution of capillary rise restrained by gravity," J. Colloid Interface Sci., vol. 320, pp. 259–263, 2008.
[99] J. L. Plawsky, A. G. Fedorov, S. V. Garimella, H. B. Ma, S. C. Maroo, L. Chen, and Y. Nam, "Nano- and Microstructures for Thin-Film Evaporation—A Review," Nanoscale Microscale Thermophys. Eng., vol. 18, no. 3, pp. 251–269, 2014.